

# FORTIFIKATORISK

NOTAT NR. 81 / 72 ✓

UNDERGROUND AMMUNITION STORAGE  
Blast propagation in the tunnel system ✓

Report III A

Single chamber storage. Variable tunnel  
diameter and variable chamber volume

DISTRIBUTION STATEMENT A  
Approved for public release;  
Distribution Unlimited

D D C  
RECEIVED  
JUL 19 1976  
RECEIVED  
D

FORSVARETS BYGNINGSTJENESTE

ADA027065

NORWEGIAN DEFENCE CONSTRUCTION SERVICE  
Office of Test and Development

White Section <input checked="" type="checkbox"/>	
Buff Section <input type="checkbox"/>	
Per Hx. on file	
CLASSIFICATION/AVAILABILITY CODES	
SPECIAL. DDD/OF SPECIAL	
A	

14

Fortifikatorisk/notat 81/72

6

UNDERGROUND AMMUNITION STORAGE.  
Blast propagation in the tunnel system.

Report III A.

Single chamber storage. Variable tunnel  
diameter and variable chamber volume.

10

A.T. Skjeltorp, T. Hegdahl and A. Jenssen

11 Jun 75

12 clp.

DDC  
RECEIVED  
JUL 19 1976  
RECEIVED  
D

RECEIVED  
JUL 19 1976  
RECEIVED

June 1975

403 636

# TABLE OF CONTENTS

Page

ABSTRACT	1
1. INTRODUCTION	2
2. THEORETICAL CONSIDERATIONS	2
2.1    Scaling Relationships	2
2.2    Peak Pressure close to Storage Chamber	4
2.3    Effects of Wall Roughness	5
3. EXPERIMENTAL DETAILS	6
4. EXPERIMENTAL RESULTS AND ANALYSIS	7
4.1    Peak Pressure Close to Storage Chamber	7
4.2    Peak Pressure Scaling Relationships	8
4.2.1    Scaling relationships for each configuration	9
4.2.2    Scaling relationships for same values of $A_j/A_c$	12
4.2.3    Scaling relationship for all configurations	12
4.2.4    Evaluation of the empirical fits	14
4.3    Scaling Relationships for Impulse	16
4.4    Scaling Relationships for Positive Duration	17
4.5    Comparison with Large Scale Tests	17
5. SUMMARY AND CONCLUSIONS	19
REFERENCES	20
Tables	
Figures	

## A B S T R A C T

Model tests have been performed to determine the blast wave propagation in the tunnel system of underground single chamber storage sites. A total of nine configurations were tested with variable tunnel diameters (6,7 - 13,5 cm), chamber volumes (7250 - 15200 cm<sup>3</sup>), and TNT loading densities (1 - 70 kg/m<sup>3</sup>).

Analysis of the blast wave data produced simple scaling relationships which contain a wide range of important geometrical parameters. Comparisons are given with one large scale test and the importance of wall roughness attenuation is discussed.



## 1. INTRODUCTION

This report is the third in a series of five /1 - 5/ describing the results from an extensive series of model tests on underground ammunition storage. In the preceeding report, (Report II A), measurements were presented on chamber pressure. The present report deals with the problem of blast wave propagation from the storage chamber down the main passage-way for typical single chamber storage sites.

The use of the present model tests in the design of underground ammunition storage sites is made possible by two special circumstances: First, the models used in the tests were designed to represent a wide range of typical full scale sites. Second, the models were carefully constructed to have sufficient strength for relatively high loading densities to cover a wide range of full scale cases.

The fundamental scaling relationships used in the tests are reviewed briefly in Sec. 2, followed by a review of the experimental details in Sec. 3. The principal experimental results are presented in Sec. 4, followed by a summary and conclusions in Sec. 5.

## 2. THEORETICAL CONSIDERATIONS

### 2.1 Scaling Relationships

The basis for the scaling relationships proposed in the present report is the familiar Hopkinson scaling laws /6/ which were reviewed in Report I /1/. However, for the present experiments various empirical cross checks have provided more general relationships. The justification for these extensions will be discussed next.

Earlier tests in straight tubes and tunnels /7/ have shown that front pressure data (disregarding wall roughness) scale approximately as

$$p = f(Q/V_t) \quad (2.1a)$$

Referring to Fig. 2.1, a),  $Q$  is the explosive charge weight and  $V_t$  the total volume traversed by the shock wave to the observation point.

Empirical fits for pressures ranging from 0,1 - 100 bar have shown that the functional relationship of Eq.(2.1a) can be approximated by (smooth wall):

$$p \simeq 24(Q/V_t)^{0,66}$$

with the units for  $Q$  and  $V_t$  in kg TNT and  $m^3$ , respectively.

Likewise, the data for positive impulse  $I$  and positive duration  $t_+$  in straight tubes and tunnels have been shown to scale approximately as (disregarding wall roughness):

$$IA/Q = g(Q/V_t) \quad (2.1b)$$

and

$$t_+ A/Q = h(Q/V_t) . \quad (2.1c)$$

Here,  $A$  is the tube or tunnel cross-sectional area.

Detonation of explosive charges at the dead end of a straight tube or tunnel, Fig. 2.1, b, will produce the same scaling relationships as in Eqs. (2.1a) - (2.1c) /7/. This geometry is of course not very different from a single chamber storage site shown in Fig. 2.1, c.

The natural extension of the scaling relationships in Eqs. (2.1a) - (2.1c) would therefore be

$$p = f(Q/V_t, A_j/A_c) \quad (2.1d)$$

$$IA_j/Q = g(Q/V_t, A_j/A_c) \quad (2.1e)$$

$$t_+ A_j/Q = h(Q/V_t, A_j/A_c) . \quad (2.1f)$$

Here,  $A_j/A_c$  is the ratio between the cross-sectional areas of the passageway and the chamber, and is introduced as a dimensionless adjustable parameter. The ratio is partly justified on the grounds that Eqs. (2.1d) - (2.1f) correctly reduce to Eqs. (2.1a) - (2.1c) for  $A_j/A_c = 1$ . It is not possible to proceed any further at this point without empirical cross-checks using the actual experimental results. In Sec. 4 various attempts will be made to test specific functional relationships of Eqs. (2.1d) - (2.1f).

Clearly, there are various aspects of the blast wave formation and propagation down the tunnel which are not accounted for by the simple scaling relationships proposed here. Some of these effects will be discussed in the following sections.

## 2.2 Peak Pressure Close to Storage Chamber

Porzel /8/ has argued that for a surface wave entering a tunnel as in Fig. 2.2a, the material velocity in the direction of the tunnel is stagnated near the entrance. The diffraction into the tunnel is then equivalent to the inverse of normal reflection, i.e. referring to Fig. 2.2a, the pressure in the tunnel,  $p_D$ , is related to the surface pressure  $p_c$ , through the usual reflection formula (ideal gas,  $\gamma = 1.4$ ):

$$p_c = \frac{2p_D(4p_D + 7)}{7 + p_D} \quad (2.2a)$$

To calculate the tunnel diffraction pressure one needs the inverse relation to Eq. (2.2a):

$$p_D = \left[ \sqrt{(14 - p_c)^2 + 224p_c} - (14 - p_c) \right] / 16 \quad (2.2b)$$

The situation discussed here is similar to the present case where the chamber pressure is diffracted into the tunnel. This hypothesis will be tested in Sec. 4.

A build-up in peak pressure over the diffraction pressure in Eq. (2.2b), is expected to occur during a few tunnel diameters ( $L/D \approx 2 - 3$ ) just inside the tunnel entrance. This is mainly due to multiple reflections and the formation of a Mach stem from numerous diffracted blast waves /8/. This build-up pressure,  $p_B$  say, has been determined empirically /8/ to be about 40% of the diffracted pressure, i.e.

$$p_B \approx 1.4 p_D \quad (2.2c)$$

It should be pointed out that the pressures discussed here are average pressures corresponding to the interpretation of average peak pressures from actual pressure-time recordings /1/.

Beyond this build-up region in the tunnel, there is a formation of a "turbulent choke". Due to the wall roughness, turbulent surface layers are formed which grow and finally converge as shown in Fig. 2.2b. When these layers collide, the material flow at the centre is stagnated. This is denoted a "turbulent choke". As the choke forms at a constant distance behind the shock front, the flow is then a steady-state phenomenon.

### 2.3 Effects of Wall Roughness

The scaling relationships in Sec. 2.1 obviously do not account for energy dissipating effects due to the tunnel walls such as

- a) thermal energy transmission to the walls
- b) elastic or inelastic deformation of the walls
- c) viscous loss due to wall roughness

This has been discussed in Report I, and it was shown that it is reasonable to assume that the energy losses in a) and b) will be relatively small compared to the total energy release. However, the loss due



to wall roughness may significantly influence the blast propagation, but only over long distances and/or in the case of large roughness. A model originally proposed by Porzel /8/ states that the peak pressure attenuation may be expressed as:

$$Y(p) = \text{constant} - 2\xi(\bar{e}/D)(L/D) \quad (2.3a)$$

Here,  $Y(p)$  is an impedance function defined as

$$Y(p) = \frac{13}{7} \ln p - \frac{6}{7} \ln(p + 7) - \frac{1}{p} \quad (2.3b)$$

with  $p$  the peak pressure at a distance  $L/D$  along the tunnel.  $\bar{e}/D$  is the average relative wall roughness, and  $\xi$  is an efficiency factor in the range  $1/2 \leq \xi \leq 1$ . For further details reference is made to the original work /8/ and Report I /1/.

For the relatively smooth-walled steel tubes used in the present tests, the effects of wall roughness are expected to be quite small. This will be discussed in more detail in Sec. 4.

### 3. EXPERIMENTAL DETAILS

Details of the models, instrumentation and data reduction are to be found in Report I /1/, and we shall therefore only summarize the main features here.

The test programme was designed to determine the blast wave propagation in a straight transport tunnel leading from a single storage chamber. A total of nine combinations of chamber volumes and tunnel cross sections were used as shown in Fig. 3.a. Most loading densities varied between 3 and 70 kg/m<sup>3</sup> and pressure-time history was recorded in most cases at six different distances from the storage chamber, ranging from approximately 2 to 80 tunnel diameters.

The pressed TNT charges used in the tests were suspended in the middle of the detonation chamber and initiated

with electrical blasting cap no. 8. This has an equivalent TNT weight of  $1,5 \pm 0,5$  g. The smallest charges used in the tests were 25 g TNT and the uncertainty in the loading density stemming from the blasting cap is therefore less than 2%. However, the total uncertainty in the loading density is estimated to be approximately 5% due to the spread in the weights of the standard TNT blocks used.

To measure the pressure-time history in the models, standard measurement techniques were used and the blast wave parameters were evaluated using special computer programmes as discussed in Report I /1/. The total uncertainty in the peak pressure determination was estimated to be typically about 10%, whereas the uncertainty in the impulse and positive duration was estimated to be about 30%. Pressure-time records obtained near the detonation chamber contained significant ringing due multiple reflected blast waves and the peak pressure determination was probably no better than approximately  $\pm 20\%$ .

#### 4. EXPERIMENTAL RESULTS AND ANALYSIS

A total of approximately 700 blast wave parameter values (peak pressure, impulse and positive duration) were obtained for the 9 configurations discussed in Sec. 3. Only the most significant results will be presented here since part B of this report contains all the pressure-time recordings and tabulated blast wave parameters.

##### 4.1 Peak Pressure Close to Storage Chamber

Pressure measurements were made near the exit of the chamber or more specifically for  $L/D = 2,5 - 2,8$  for all the configurations listed in Fig. 3.a. These results are shown in Fig. 4.1a - 4.1c.

The dashed lines  $p_c$  in these figures are the average peak chamber pressures versus loading density

which have been presented in Report II A /2/.

The solid lines  $p_D$  are the theoretical prediction of the diffracted pressure using Eq.(2.2b) and the dotted lines  $p_B$  the diffracted build-up pressure using both Eqs.(2.2b) and (2.2c). As may be seen there is fair agreement between the measurements and the  $p_B$ -curves considering the rough approximations made in the theoretical predictions and the uncertainties involved in the interpretation of the average peak pressures from measurements. It may be noted that the experimental data appear to be increasingly higher in relation to the  $p_B$ -curves for decreasing values of  $A_j/A_c$ . This may be due to an increased build-up pressure for smaller  $A_j/A_c$ -values.

The same tendency appears to be the case also for increasing chamber volumes. However, within approximately  $\pm 30\%$  the experimental data are reproduced by the theoretical curves.

#### 4.2 Peak Pressure Scaling Relationships

The basic quantity of interest in the present model tests is the peak side-on overpressure  $p$  in the passageway. In Fig. 4.2a,  $p$  is plotted versus  $L/D$  with the loading density  $Q/V_i$  as parameter for one typical configuration. Fig. 4.2b shows the same data plotted versus  $Q/V_i$  with  $L/D$  as parameter. These plots are in so-called dimensionless form, i.e. independent the linear scaling factor  $n$ . (See Report I /1/).

Letting subscripts F and M denote full scale and model respectively,

$$p_F = p_M, \quad (4.2a)$$

$$\text{and } L_F/D_F = nL_M/nD_M = L_M/D_M.$$

For the loading density,

$$Q_F/V_F = n^3Q_M/n^3V_M = Q_M/V_M \quad (4.2b)$$



The results in Figs. 4.2a and 4.2b may therefore in principle be used for any geometrically similar systems. However, it is of interest to reduce the number of curves necessary to characterize the blast wave propagation in this particular system. In Sec. 2.2, it was proposed to scale the data according to  $Q/V_t$ , where now  $V_t$  is the total volume of the chamber and the tunnel out to the observation point. Fig. 4.2c shows the results in this presentation for the same data as before. As may be seen, the data points are evenly distributed around one straight line. This means that one universal curve appears to reproduce the tunnel pressure at any point in the tunnel for any charge  $Q$  for the present range of measurements. In particular, it is remarkable to note that even the data for  $L/D = 2,8$  in Fig. 4.2c, appear to fall together with the bulk of the data for  $L/D > 10$ .

Figs. 4.2d - 4.2f show the variation of  $p$  versus  $Q/V_t$  for all the data grouped together for the same value of  $A_j/A_c$  with  $V_i$  as parameter. As may be seen, there appear to be no distinct systematic differences between the three sets of data for the three different chamber volumes. However, there is a systematic lowering of the bulk of the data points for decreasing values of  $A_j/A_c$ . These observations will be tested more systematically in the following sections which contains the results from various empirical fits of all the data to the general relationship in Eq. (2.1d). Special computer programs were used for this purpose, and for details reference is made to Report I /1/.

#### 4.2.1 Scaling Relationships for Each Configuration

This section lists three methods examined for scaling the peak pressure data for each of the nine configurations of the tests.



Method a

The first method of scaling that was investigated is based on the empirical observation made in Sec. 4.2. Here, it was shown that for one configuration,  $\log p$  varied approximately linearly with  $\log (Q/V_t)$ .

Matematically, this can be expressed as

$$p = B_1(Q/V_t)^{B_2} \quad (4.2.1a)$$

where:

- $p$  = measured peak pressure
- $Q/V_t$  = effective loading density
- $B_1$  = scaling factor
- $B_2$  = scaling exponent

The computer program made least squares fits of all the data to Eq.(4.2.1a) for each of the nine configurations  $(A_1, V_1), (A_1, V_2), \dots$  in Fig. 3.a to determine  $B_1$  and  $B_2$ .

The results of this procedure are shown in Table 4.2.1a. As may be seen, there appears to be no systematic variations in  $B_1$  for different chamber volumes for the same value of  $A_j/A_c$ . However, on the average there is a relatively small increase in the values of  $B_2$  for increasing chamber volumes. For decreasing values of  $A_j/A_c$ , there is on the average a distinct systematic decrease in  $B_1$  whereas  $B_2$  increases somewhat.

Method b

The second method used to scale the peak pressures is also based on Eq. (4.2.1a), but including also the possibility of wall roughness attenuation employing the impedance function  $Y(p)$  discussed in Sec. 2.3:

$$p_o = C_1(Q/V_t)^{C_2} \quad (4.2.1b)$$

$$Y(p_o) - Y(p) = (C_3/D)(L/D) \quad (4.2.1c)$$

where:

$p_o$  = fictitious peak pressure without wall friction

$p$  = measured peak pressure

$Y(p_o)$  = impedance function of  $p_o$ , Eq.(2.3b)

$Y(p)$  = impedance function of  $p$ , Eq. (2.3b)

$C_1$  = scaling factor

$C_2$  = scaling exponent

$C_3$  =  $2 \xi \bar{e}$  = effective wall roughness, see Report I.

As in method a), the data for each of the nine configurations were fitted to Eqs.(4.2.1b) and (4.2.1c). The results of this procedure are shown in Table 4.2.1b. As may be seen, the scaling parameters  $C_1$  and  $C_2$  do not differ significantly from the earlier values for  $B_1$  and  $B_2$  in Table 4.2.1a. The effective wall roughness  $C_3$  is on the average quite small which is consistent with the use of the relatively smooth-walled steel tubes in the tests.

#### Method c

The third method used was identical to method b) except for introducing an additional parameter  $D_4$ :

$$p_o = D_1(Q/V_t - D_4)^{D_2} \quad (4.2.1d)$$

$$Y(p_o) - Y(p) = (D_3/D)(L/D) \quad (4.2.1e)$$

The use of  $D_4$  is a crude way to check the possible effects of the oxygen deficiency in TNT /2/.

Again, the data for each of the nine configurations were fitted to Eqs.(4.2.1d) and (4.2.1e). The results of this procedure are shown in

Table 4.2.1c. As may be seen, there are significant variations in the fitted values for  $D_4$ , introducing large variations in the other scaling parameters.

#### 4.2.2 Scaling Relationships for Same Values of $A_j/A_c$

This section lists three methods examined for scaling the combined peak pressure data for  $V_1$ ,  $V_2$ , and  $V_3$  for each value of  $A_j/A_c$ . This was partly justified from the findings in Sec. 4.2, which showed that the fitted scaling parameters appeared to be relatively insensitive to the variation in the chamber volume. The form of the scaling relationships were identical to those tested in Sec. 4.2.1.

##### Method a

The use of Eq. (4.2.1a) produced the set of scaling parameters shown in Table 4.2.2a. (Note that the scaling parameters now are denoted  $E_1$  and  $E_2$  instead of  $B_1$  and  $B_2$ ). The systematic variation of  $E_1$  and  $E_2$  with  $A_j/A_c$  is evident.

##### Method b

The use of Eqs. (4.2.1b) and (4.2.1c) produced the set of scaling parameters shown in Table 4.2.2b (C's replaced by F's). As before, the effective wall roughness  $F_3$  is small as it should.

##### Method c

The use of Eqs. (4.2.1d) and (4.2.1e) produced the set of scaling parameters shown in Table 4.2.2c. (D's replaced by G's). The large variations in  $G_4$  produce large scatter in the other scaling parameters.

#### 4.2.3 Scaling Relationship for All Configurations

This section lists three methods examined for scaling all the peak pressure data at once including also the effects from the variation of  $A_j/A_c$  in the fits.

Method a

The first method is essentially the same as method a) in Secs. 4.2.1 and 4.2.2 except for introducing an additional parameter  $H_5$ :

$$p = H_1(Q/V_t)^{H_2} (A_j/A_c)^{H_5} \quad (4.2.3a)$$

The use of  $H_5$  is a way to find an empirical dependence of  $p$  on  $A_j/A_c$ . The results from this fitting procedure are shown in Table 4.2.3a. As may be seen, the fitted value for  $H_5$  is quite uncertain.

Method b

The second method is essentially the same as method b) in Secs. 4.2.1 and 4.2.2 except for introducing the  $A_j/A_c$ -dependence:

$$p_o = J_1(Q/V_t)^{J_2} (A_j/A_c)^{J_5} \quad (4.2.3b)$$

$$Y(p_o) - Y(p) = (J_3/D)(L/D) \quad (4.2.3c)$$

The results of this fitting procedure are shown in Table 4.2.3b. There is a considerable improvement in the fitted parameters compared to method a).

Method c

The third and last method is again essentially the same as method c) in Secs. 4.2.1 and 4.2.2 except for introducing the  $A_j/A_c$ -dependence:

$$p_o = J_1(Q/V_t - J_4)^{J_2} (A_j/A_c)^{J_5} \quad (4.2.3d)$$

$$Y(p_o) - Y(p) = (J_3/D)(L/D) \quad (4.2.3e)$$



The result of this fitting procedure are shown in Table 4.2.3c. The introduction of the parameter  $J_5$  causes minor changes in the other parameters compared to method b).

#### 4.2.4 Evaluation of the Empirical Fits

On the basis of the results from the nine different empirical fits found in the preceeding sections, there are three major conclusions which may be reached:

- i) The nine different scaling relationships all reproduce the data within approximately twice the expected experimental scatter ( $\pm 20\%$ ). There are only minor differences for the different methods in the data scatter around the fitted curves.
- ii) Methods b) and c) involving the use of the proposed impedance function, have produced relatively small empirical values for the average wall roughness. This is consistent with the relatively smooth-walled steel tubes used in the tests.
- iii) The introduction of an additional parameter ( $D_4$ ,  $G_4$ ,  $I_4$ ) in method c) to see the possible effects of the oxygen deficiency in TNT, did not improve the fits.

As a general conclusion it is therefore recommended to use the results in Table 4.2.3b in the prediction of the smooth wall peak pressures, i.e.:

$$p_o = (12,1 \pm 0,6)(Q/V_t)^{0,607 \pm 0,016} (A_j/A_c)^{0,19 \pm 0,04} \dots (4.2.4)$$

Here, a  $2\sigma$  standard deviation (96% confidence interval) has been used on the scaling parameters. Eq. (4.2.4) has reproduced all the data with an average error of approximately 14%. This is quite satisfactory considering the estimated 10% experimental uncertainty in the peak pressure determination.

There are four major limitations imposed on the present results for which the simple relationship in Eq. (4.2.4) is expected to be invalid; a) different geometry of the chamber exit; b) long chambers; c) short distances from the chamber exit ( $L/D \rightarrow 0$ ); and d) significant wall roughness. In regard to case a), earlier shock tube experiments have shown that abrupt cross-section changes (i.e. sharp corners as in the present tests) attenuate the blast wave much more than smooth transitions /9/. As for case b), long chambers would allow the blast wave to travel in both directions if the charge was placed in the middle of the chamber and a double-peaked blast wave would be observed in the tunnel. One peak would be due to the direct blast wave and the second due to the reflected wave off of the back wall of the chamber. In case c) the complicated reflection pattern of the blast wave going from the chamber to the tunnel precludes any unambiguous definition of a peak pressure.

For significant tunnel wall roughness, case d), Eq. (4.2.4) may be supplemented by the use of the impedance function as outlined earlier in this section and in Report I /1/. As has been discussed elsewhere /10/, the wall roughness attenuation may be considerable for typical tunnels blasted out of rock, and the use of Eq. (4.2.4) will be quite conservative or on the safe side.

#### 4.3 Scaling Relationships for Impulse

The results for the impulse are much more difficult to combine empirically in a straightforward way than those for the front pressure. This is partly due to the significantly larger uncertainties involved here and special features are not easily discernible. This is clear from the typical results in Fig. 4.3a. On the average, the impulse decreases slowly with distance from the storage chamber, but there is no systematically large drop near the chamber as was observed for front pressure.

To test the proposed scaling hypothesis in Sec. 2.1, Eq. (2.1.e), the results for the impulse measurements are shown in Figs. 4.3b - 4.3j as  $I A_j/Q$  versus  $Q/V_t$ . As expected, the data show relatively large scatter, but to a first approximation the results fall on discrete curves with  $L/D$  as a parameter. Part, or all of the  $L/D$  dependence may be due to the wall roughness, but so far it has not been possible to account for this theoretically. The results also show that the scaled impulse is relatively insensitive to the values for  $A_j/A_c$  and the chamber volume  $V_i$ . As for front pressure, various empirical scaling relationships with Eq. (2.1e) as basis were fitted to the experimental results. In particular, a reasonable fit to all the data was obtained using the following expression:

$$I A_j/Q = K_1 (Q/V_t)^{K_2} (A_j/A_c)^{K_3} \exp(-K_4 \cdot L/D) \dots (4.3)$$

Here,  $K_1$ ,  $K_2$ ,  $K_3$ , and  $K_4$  were introduced as scaling parameters. The result of this procedure are shown in Table 4.3. As expected, the scaling parameters are relatively uncertain, but Eq. (4.3) reproduces all the data with an average scatter of approximately 25 %. This is quite satisfactory considering the relatively large uncertainties involved in the interpretation of the impulse.

The simple relationship in Eq. (4.3) is expected to be invalid for the same cases as listed in Sec. 4.2.4 for the peak pressure data. For significant wall roughness as for tunnels blasted out of rock, the use of Eq. (4.3) will probably produce result which are quite conservative or on the safe side.

#### 4.4. Scaling Relationships for Positive Duration.

The results and the interpretation of the positive duration data show similar characteristics as for the impulse data discussed in Sec. 4.3. The comments made there essentially also apply here. Some typical results are shown in Fig. 4.4. Again, there is large scatter in the data, but to a first approximation the results fall in discrete curves with  $L/D$  as parameter. As for the impulse data, a reasonable fit to all the data was obtained using an expression:

$$t_+ A_j / Q = L_1 (Q/V_t)^{L_2} (A_j/A_c)^{L_3} \exp(-L_4 L/D) \quad (4.4)$$

Here,  $L_1$ ,  $L_2$ ,  $L_3$  and  $L_4$  act as scaling parameters. The results of the nonlinear least squares fit of Eq. (4.4) to all the data are shown in Table 4.4. This fit reproduces all the results with an average scatter of approximately 30 % which again is quite satisfactory considering the large uncertainties involved in the interpretation of the experimental results. The limitations are essentially the same as those listed in Sec. 4.2.4 for the peak pressure data.

#### 4.5. Comparison with Large Scale Tests.

Parts of some large scale tests performed by the Norwegian Defence Research Establishment (NDRE) /11/, correspond approximately to the model tests reported



here. TNT charges ranging from 100 to 1000 kg were positioned at a blind end of a rock tunnel with a cross section of  $5,5 \text{ m}^2$ . The pressure was recorded at 6 different distances from the charge ranging from 20 to 80 m as shown in Fig. 4.5a. This situation would correspond to the special case where  $A_j/A_c = 1$ .

However, as indicated in Fig. 4.5a, a side chamber is connected to the tunnel, and this will obviously attenuate the blast wave somewhat, but probably less than 20 % /9/. Fig. 4.5b shows peak pressure versus effective loading density with the distance from the charge in tunnel diameters,  $L/D$ , as parameter. As may be seen, these results are consistently lower than the model data for  $A_j/A_c = 0,45$ . Moreover, the large scale data show a pronounced  $L/D$ -dependence which is undoubtedly due to the wall roughness attenuation which was discussed earlier.

Employing the impedance function discussed earlier, the large scale data in Fig. 4.5b were fitted to Eqs. (4.2.1b) and (4.2.1c), which produced a "smooth wall" relationship:

$$p_o = (12 \pm 2)(Q/V_t)^{0,57 \pm 0,04} \quad (4.5a)$$

and an effective wall roughness

$$2 \xi \bar{e} = 0,19 \pm 0,02 \text{ m} \quad (4.5b)$$

The corrected "smooth wall" data  $p_o$  are shown in Fig. 4.5c together with the fitted curve expressed by Eq. (4.5a).

Even the "smooth wall" data are consistently lower than the corresponding model data, which may be due to additional losses in the full scale case as large amounts of water was present. This will be discussed in more detail in Report V in connection with other large scale tests in the same installation.

## 5. SUMMARY AND CONCLUSIONS

The methods in this report for the prediction of blast wave propagation in single chamber storage sites constitute a major source of information in the planning of full scale installations in rock.

The results provide a simple and sufficiently accurate method for the determination of the blast wave parameters at any point in the transport tunnel for a wide range of loading densities and geometries. This is made possible by the use of simple scaling relationships with the following characteristics:

- a) All the formulas are given in dimensionless form independent of scale.
- b) The net explosive quantity (TNT) is used as basic input parameter.
- c) The effects from a wide range of geometrical configuration (chamber volumes, tunnel cross-sections) have been introduced in a relatively simple form.
- d) The results are valid for essentially smooth-walled tunnels and are expected to be conservative or on the safe side for tunnels blasted out of rock.
- e) The scaling relationship for the peak pressure data may serve as a starting point for the prediction of the blast reducing effects of wall roughness.

Direct comparisons of the present results have been made with one large scale test with a similar tunnel system, but with a much larger relative wall roughness. The relatively large difference in the peak pressure attenuation for the model and large scale tests, has been partly accounted for as being due to the difference in wall roughness.

Finally, it is believed that this study, with its method for the prediction of blast at the tunnel exit, is a promising starting point in the determination of the hazardous area around an underground ammunition storage site.

## REFERENCES

1. A. Skjeltnorp, T. Hegdahl, and A. Jenssen,  
"Underground Ammunition Storage I: Test program,  
instrumentation and data reduction".  
Technical note no 80/72, Norwegian Defence Construction  
Service (1975).
2. A. Skjeltnorp, T. Hegdahl, and A. Jenssen,  
"Underground Ammunition Storages II A and II B:  
Chamber Pressure", Technical note no 79/72, Norwegian  
Defence Construction Service (1975).
3. A. Skjeltnorp, T. Hegdahl, and A. Jenssen,  
"Underground Ammunition Storages IV A and IV B:  
Connected chamber storage with variable chamber volume  
and variable angle between branch and main passageway."  
Technical note no 82/72, Norwegian Defence Construc-  
tion Service (1975).
4. A. Skjeltnorp, T. Hegdahl, and A. Jenssen,  
"Underground Ammunition Storage V A and V B: Connected  
chamber storage. Blast load on doors in two sites."  
Technical note no 83/72, Norwegian Defence Construc-  
tion Service (1975).
5. The reports in Refs 2-4 labeled A contain the main  
results whereas the reports labeled B contain the raw  
data in the form of pressure-time recordings and  
tabulated blast wave parameters.
6. See for example W.E. Baker, P.S. Westine, and F.T. Dodge,  
"Similarity Methods in Engineering Dynamics" (Hyden  
Book Co., New Jersey, U.S. A., 1973) Ch.4.
7. A.T. Skjeltnorp and A. Jenssen,  
"One dimensional Blast Wave Propagation".  
4th International Symposium on Military Application  
of Blast Simulation. (1974).
8. F.B. Porzel,  
"Study of Schock Impedance Effects in a Rough Walled  
Tunnel", Research Paper No. P-330, Institute for  
Defence Analysis (1969) (AD 684790).
9. W.J. Taylor,  
"Blast Wave Behavior in Confined Regions", Annuals of  
the New York Academy of Sciences, vol. 152, p. 339  
(1968).
10. A.T. Skjeltnorp,  
"Airblast Propagation Through Tunnels and the Effects  
of Wall Roughness", Technical note no. 103/75,  
Norwegian Defence Construction Service (1975).
11. K.G. Schmidt,  
"Underground Explosion Trials at Raufoss 1968: Blast  
Wave Propagation Following a Detonation in a Tunnel  
System", Norwegian Defence Research Establishment,  
Report no. X-128 (1970).

Table 4.2.1a Least squares fits of Eq. (4.2.1a) to the peak pressure data for each of the nine test configurations.

$V_i$ (cm <sup>3</sup> )	$A_j/A_c$	$B_1^a$	$B_2$	Error <sup>b</sup> (%)
7250	0,45	14,4 ± 1,0	0,43 ± 0,02	6
10900	0,45	11,6 ± 1,1	0,51 ± 0,02	11
15200	0,45	10,3 ± 1,1	0,62 ± 0,02	12
7250	0,23	10,0 ± 1,1	0,52 ± 0,02	9
10900	0,23	7,7 ± 1,1	0,64 ± 0,02	10
15200	0,23	8,5 ± 1,1	0,66 ± 0,02	10
7250	0,11	6,9 ± 1,1	0,64 ± 0,02	10
10900	0,11	6,7 ± 1,1	0,71 ± 0,02	8
15200	0,11	7,1 ± 1,1	0,70 ± 0,02	13

<sup>a</sup> In units where  $p$  is expressed in bar,  $Q$  in kg TNT, and  $V_t$  in m<sup>3</sup>.

<sup>b</sup> Average difference between fitted curve and experimental data.



Table 4.2.1b. Nonlinear least squares fits of Eqs. (4.2.1b) and (4.2.1c) to the peak pressure data for each of the nine test configurations.

$V_i$ (cm <sup>3</sup> )	$A_j/A_c$	$C_1^a$	$C_2$	$C_3$ (mm)	Error <sup>b</sup> (%)
7250	0,45	11,7 ± 1,2	0,50 ± 0,04	0,0 ± 0,3	12
10900	0,45	10,0 ± 0,9	0,58 ± 0,03	0,1 ± 0,3	15
15200	0,45	10,0 ± 0,7	0,63 ± 0,02	0,0 ± 0,3	13
7250	0,23	10,7 ± 0,7	0,51 ± 0,02	0,22 ± 0,14	9
10900	0,23	8,4 ± 0,7	0,63 ± 0,02	0,17 ± 0,12	9
15200	0,23	9,6 ± 0,6	0,64 ± 0,02	0,31 ± 0,11	9
7250	0,11	6,9 ± 0,6	0,63 ± 0,02	0,00 ± 0,07	10
10900	0,11	7,0 ± 0,8	0,71 ± 0,03	0,11 ± 0,09	8
15200	0,11	7,8 ± 0,6	0,680 ± 0,018	0,13 ± 0,08	13

<sup>a</sup> In units where p is expressed in bar, Q in kg, and  $V_t$  in m<sup>3</sup>.

<sup>b</sup> Average difference between fitted curve and experimental data.

Table 4.2.1c. Nonlinear least squares fits of Eqs.(4.2.1d) and (4.2.1e) to the peak pressure data for each of the nine test configurations.

$V_i$ ( $\text{cm}^3$ )	$A_j/A_c$	$D_1^a$	$D_2$	$D_3$ (mm)	$D_4$ ( $\text{kg}/\text{m}^3$ )	Error <sup>b</sup> (%)
7250	0,45	$15,9 \pm 1,0$	$0,39 \pm 0,04$	$0,00 \pm 0,17$	$0,31 \pm 0,14$	6
10900	0,45	$9,9 \pm 1,5$	$0,56 \pm 0,06$	$0,0 \pm 0,4$	$0,06 \pm 0,10$	16
15200	0,45	$10,4 \pm 1,2$	$0,58 \pm 0,05$	$0,0 \pm 0,3$	$0,16 \pm 0,08$	16
7250	0,23	$13,5 \pm 0,9$	$0,43 \pm 0,03$	$0,25 \pm 0,11$	$0,30 \pm 0,08$	8
10900	0,23	$7,1 \pm 1,4$	$0,68 \pm 0,04$	$0,15 \pm 0,12$	$-0,3 \pm 0,2$	9
15200	0,23	$9,9 \pm 1,3$	$0,64 \pm 0,04$	$0,31 \pm 0,11$	$0,05 \pm 0,19$	9
7250	0,11	$6,8 \pm 1,4$	$0,64 \pm 0,04$	$0,00 \pm 0,07$	$0,0 \pm 0,3$	10
10900	0,11	$9,7 \pm 1,8$	$0,60 \pm 0,06$	$0,03 \pm 0,07$	$0,8 \pm 0,5$	6
15200	0,11	$4,2 \pm 1,0$	$0,87 \pm 0,03$	$0,18 \pm 0,07$	$-1,31 \pm 0,16$	10

<sup>a</sup> In units where p is expressed in bar, Q in kg TNT, and  $V_t$  in m<sup>3</sup>.

<sup>b</sup> Average difference between fitted curve and experimental data.

Table 4.2.2a. Least squares fits of Eq. (4.2.1a) to the combined peak pressure data for all three chamber volumes for each value of  $A_j/A_c$ .

$A_j/A_c$	<sup>a</sup>		<sup>b</sup>
	$E_1$	$E_2$	Error (%)
0,45	$11,6 \pm 1,0$	$0,535 \pm 0,015$	12
0,23	$8,8 \pm 1,0$	$0,601 \pm 0,015$	13
0,11	$6,9 \pm 1,0$	$0,680 \pm 0,014$	12

<sup>a</sup> In units where  $p$  is expressed in bar,  $Q$  in kg TNT, and  $V_t$  in  $m^3$ .

<sup>b</sup> Average difference between fitted curve and experimental data.

Table 4.2.2b. Nonlinear least squares fits of Eqs. (4.2.1b) and (4.2.1c) to the combined peak pressure data for all three chamber volumes for each value of  $A_j/A_c$ .

$A_j/A_c$	$F_1$	$F_2$	$F_3$ (mm)	Error (%)
0,45	$11,3 \pm 0,5$	$0,543 \pm 0,016$	$0,00 \pm 0,16$	13
0,23	$9,7 \pm 0,5$	$0,588 \pm 0,015$	$0,22 \pm 0,09$	12
0,11	$7,3 \pm 0,4$	$0,667 \pm 0,014$	$0,06 \pm 0,05$	12

<sup>a</sup> In units where  $p$  is expressed in bar,  $Q$  in kg TNT, and  $V_t$  in  $m^3$ .

<sup>b</sup> Average difference between fitted curve and experimental data.



Table 4.2.2c. Nonlinear least squares fits of Eqs. (4.2.1d) and (4.2.1e) to the combined peak pressure data for  $V_1$ ,  $V_2$ , and  $V_3$  for each value of  $A_j/A_c$ .

$A_j/A_c$	$G_1$	$G_2$	$G_3$	$G_4$	Error
			(mm)	(kg/m <sup>3</sup> )	(%)
0,45	10,3 ± 0,9	0,57 ± 0,03	0,0 ± 0,2	0,14 ± 0,06	18
0,23	9,9 ± 0,8	0,58 ± 0,02	0,22 ± 0,09	0,03 ± 0,08	12
0,11	5,1 ± 0,8	0,78 ± 0,03	0,06 ± 0,05	-0,77 ± 0,14	12

a In units where  $p$  is expressed in bar,  $Q$  in kg TNT, and  $V_t$  in m<sup>3</sup>.

b Average difference between fitted curve and experimental data.

Table 4.2.3a. Nonlinear least squares fits of Eq. (4.2.3a) to the combined peak pressure data for all the configurations. The average difference between the empirical curves and experimental data is 19%.

Parameter	Numerical value
$H_1^a$	$7,6 \pm 0,8$
$H_2$	$0,68 \pm 0,03$
$H_5$	$0,03 \pm 0,04$

<sup>a</sup> In units where p is expressed in bar, Q in kg TNT and  $V_t$  in  $m^3$ .

Table 4.2.3b. Nonlinear least squares fit of Eqs. (4.2.3b) and (4.2.3c) to the combined peak pressure data of all the configurations. The average difference between the fitted curve and experimental data is 14%.

Parameter	Numerical value
$I_1^a$	12,1 $\pm$ 0,3
$I_2$	0,607 $\pm$ 0,008
$I_3$	0,00 $\pm$ 0,05 (mm)
$I_5$	0,19 $\pm$ 0,02

<sup>a</sup> In units where p is expressed in bars, Q in kg TNT, and  $V_t$  in  $m^3$ .

Table 4.2.3c. Nonlinear least squares fit of Eqs. (4.2.3d) and (4.2.3e) to the combined peak pressure data of all the configurations. The average difference between the fitted curves and experimental data is 14%.

Parameter	Numerical value
<sup>a</sup> $J_1$	$11,5 \pm 0,5$
$J_2$	$0,624 \pm 0,014$
$J_3$	$0,00 \pm 0,05 \text{ (mm)}$
$J_4$	$-0,08 \pm 0,05 \text{ (kg/m}^3\text{)}$
$J_5$	$0,19 \pm 0,02$

<sup>a</sup> In units where p is in bar, Q in kg TNT, and  $V_t$  in  $m^3$ .



Table 4.3. Nonlinear least squares fit of Eq. (4.3) to the combined impulse data of all the configurations. The average difference between the fitted curve and experimental data is 25%.

Parameter	Numerical value
<sup>a</sup> $K_1$	30,2 $\pm$ 1,5
$K_2$	- 0,33 $\pm$ 0,02
$K_3$	- 0,02 $\pm$ 0,04
$K_4$	0,0160 $\pm$ 0,0011

<sup>a</sup> In units where I is in bar ms, Q in kg TNT,  $A_j$  in  $m^2$  and  $V_t$  in  $m^3$ .

Table 4.4. Nonlinear least squares fit of Eq. (4.4) to the combined positive duration data of all the configurations. The average difference between the fitted curve and experimental data is 31%.

Parameter	Numerical value
<sup>a</sup> $L_1$	20,3 $\pm$ 1,1
$L_2$	- 0,81 $\pm$ 0,03
$L_3$	0,16 $\pm$ 0,03
$L_4$	0,0211 $\pm$ 0,0009

<sup>a</sup> In units where  $t_+$  is in ms, Q in kg TNT,  $A_j$  in  $m^2$  and  $V_t$  in  $m^3$ .

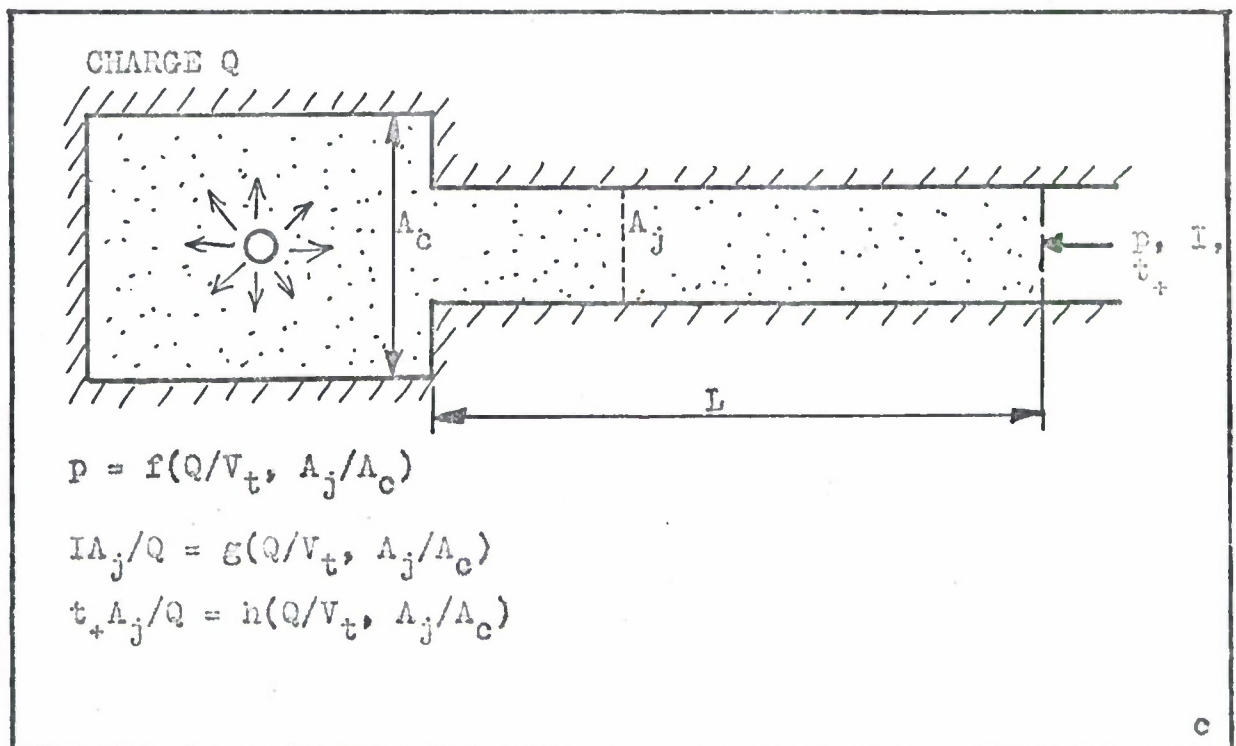
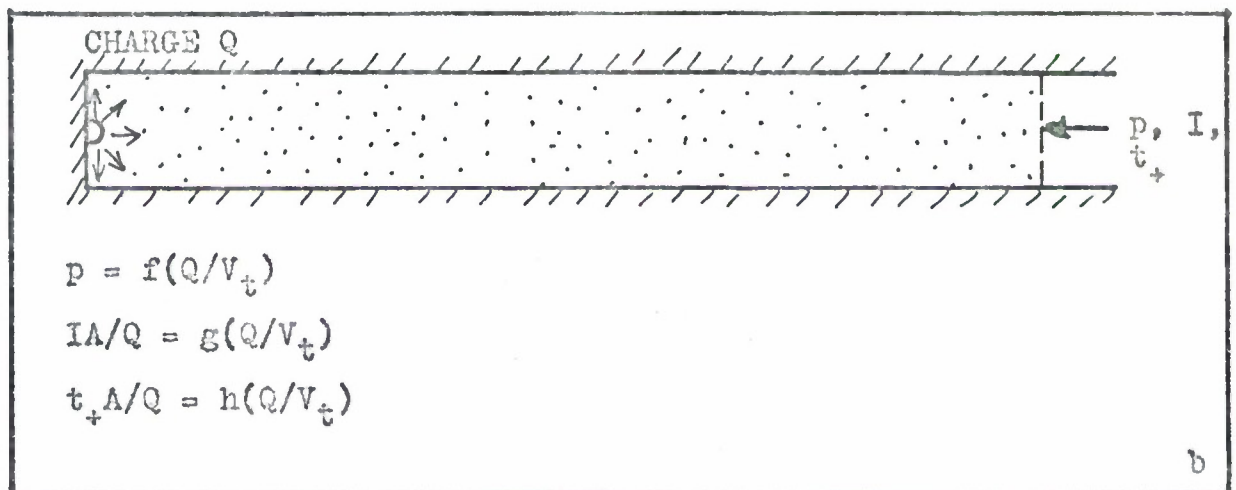
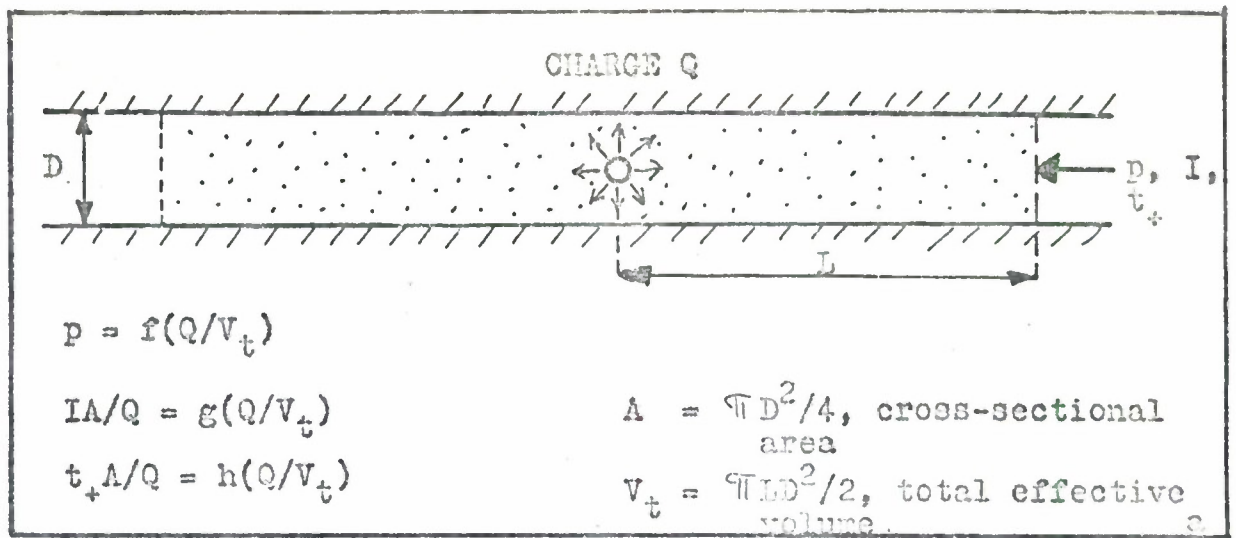


Fig. 2.1. Proposed extension of scaling relationships for single chamber storage sites in c) from scaling relationships in straight tunnels, a) and b).

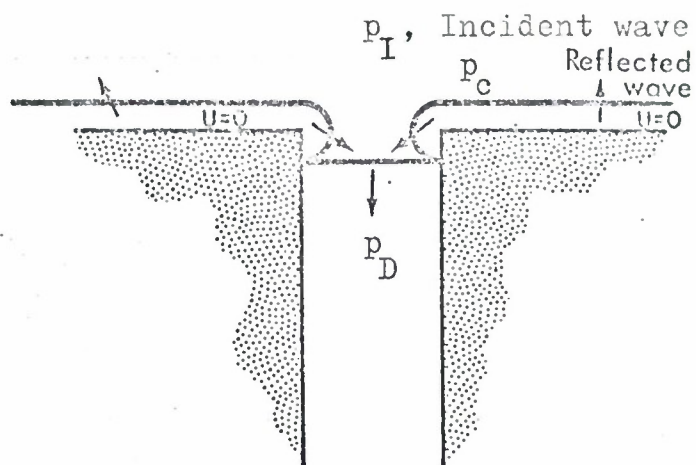
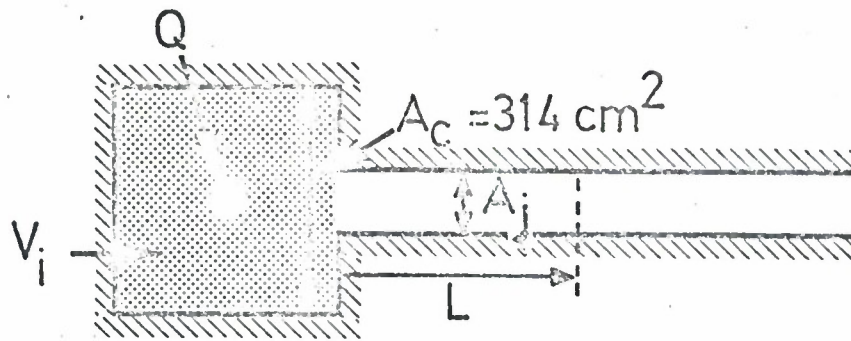


Fig. 2.2a Diffraction of a surface blast wave entering a tunnel /8/.



Fig. 2.2b Blast wave propagation in a tunnel with the formation of a turbulent choke /8/.





i	$V_i$ (cm <sup>3</sup> )	$V_i^F$ (m <sup>3</sup> )	j	$A_j$ (cm <sup>2</sup> )	$A_j^F$ (m <sup>2</sup> )	n
1	7250	380-3100	1	35	20	75
2	10900	580-4700	2	70	20	53
3	15200	800-6500	3	140	20	38

Fig.3.a. Model configurations used in the single chamber storage tests. The three chamber volumes  $V_i$  and the three tunnel cross-sections  $A_j$  given in the table thus formed nine combinations of  $V_i A_j$  with  $i = 1, 2, 3$  and  $j = 1, 2, 3$ .

Choosing  $A_j^F = 20 \text{ m}^2$  as a typical full scale value for the tunnel cross-section, the linear scaling factors  $n$  have the values shown in the last column. The corresponding full scale chamber volumes are  $V_i^F$ .

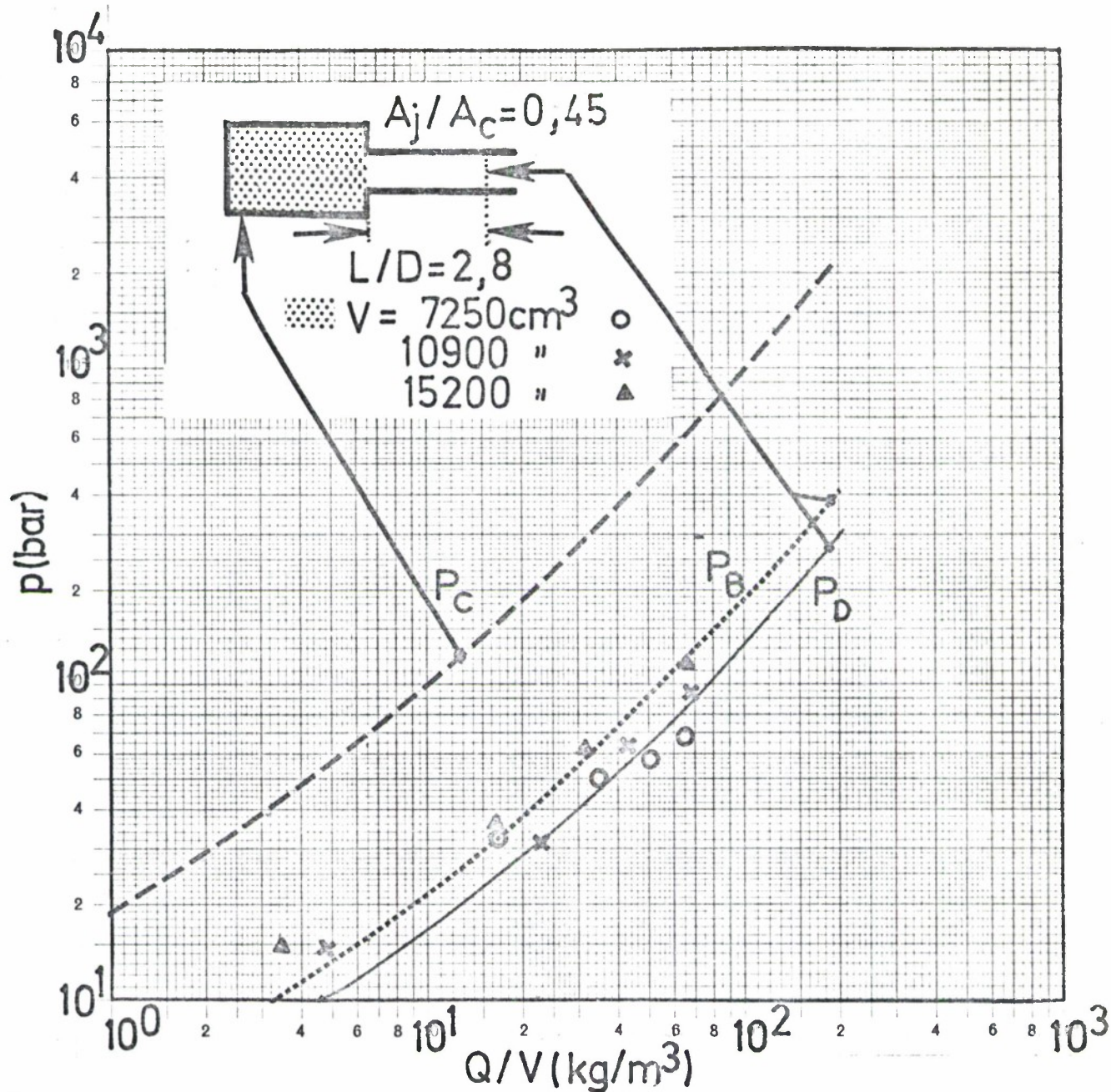


Fig. 4.1a Peak pressure near the chamber exit versus loading density for three chamber volumes. The ratio between the tunnel and chamber cross-sections is  $A_j/A_c = 0,45$ .

The dashed line represents the average peak chamber pressure,  $p_c$ , determined earlier [2/], and the solid line,  $p_D$  is determined from the inverse reflection formula in Eq.(2.2b). The dotted line is the diffracted build-up pressure,  $p_B$ , using both Eqs. (2.2b) and (2.2c).



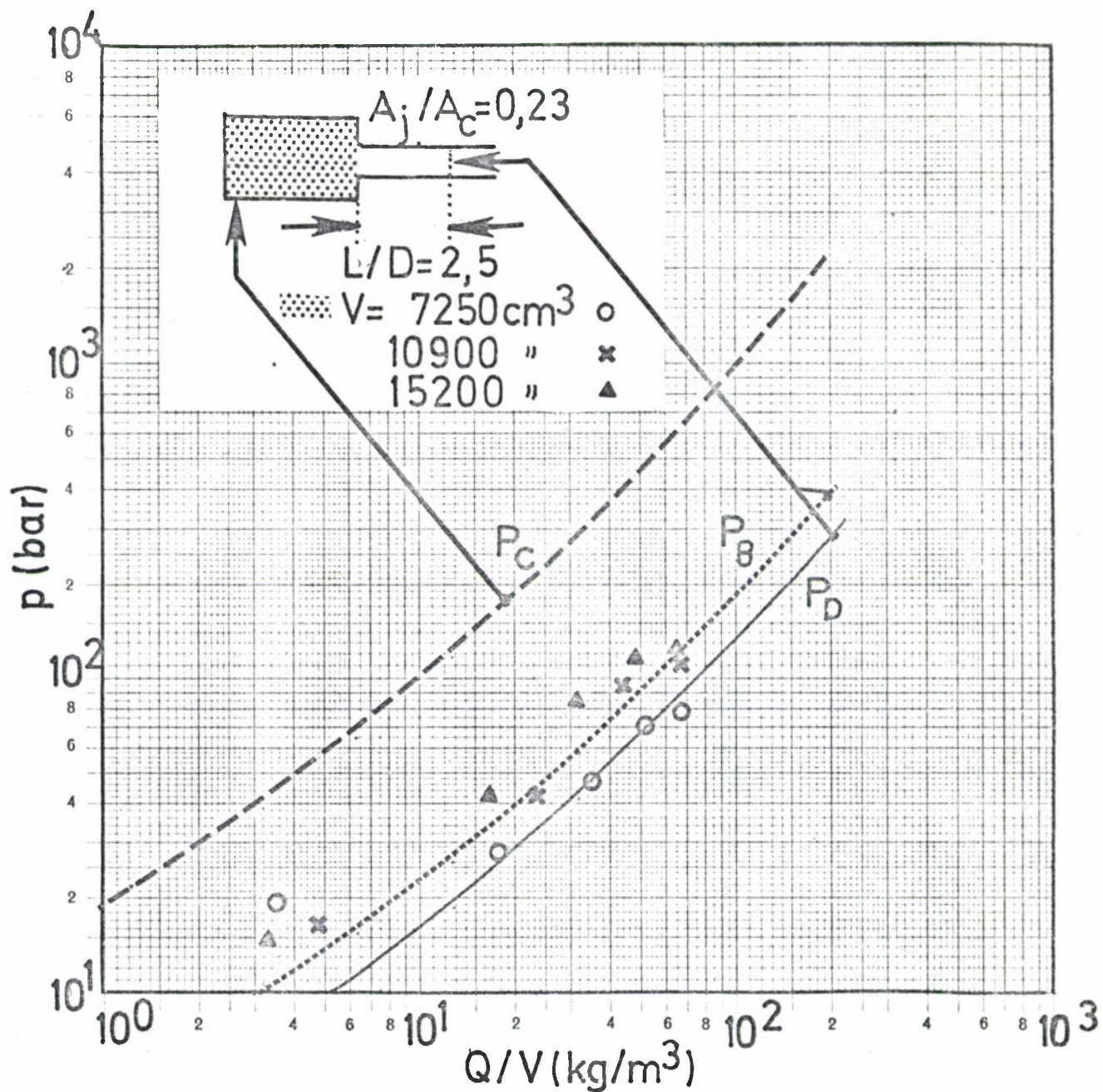


Fig. 4.1b Peak pressure near chamber exit versus loading density for  $A_j/A_c = 0,23$  (See Fig. 4.1a for details).

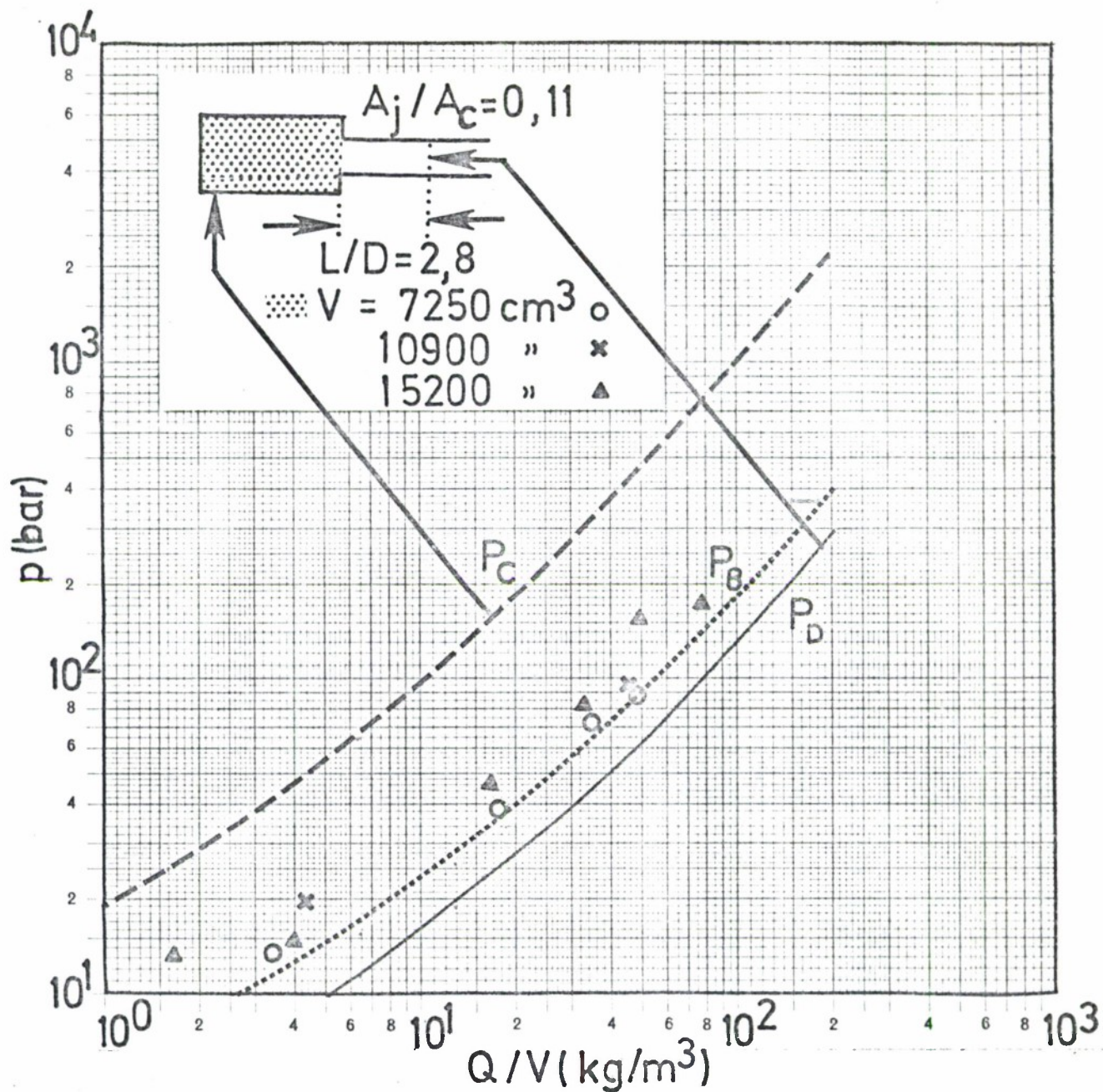


Fig. 4.1c Peak pressure near chamber exit versus loading density for  $A_j/A_c = 0,23$  (See Fig 4.1a for details).





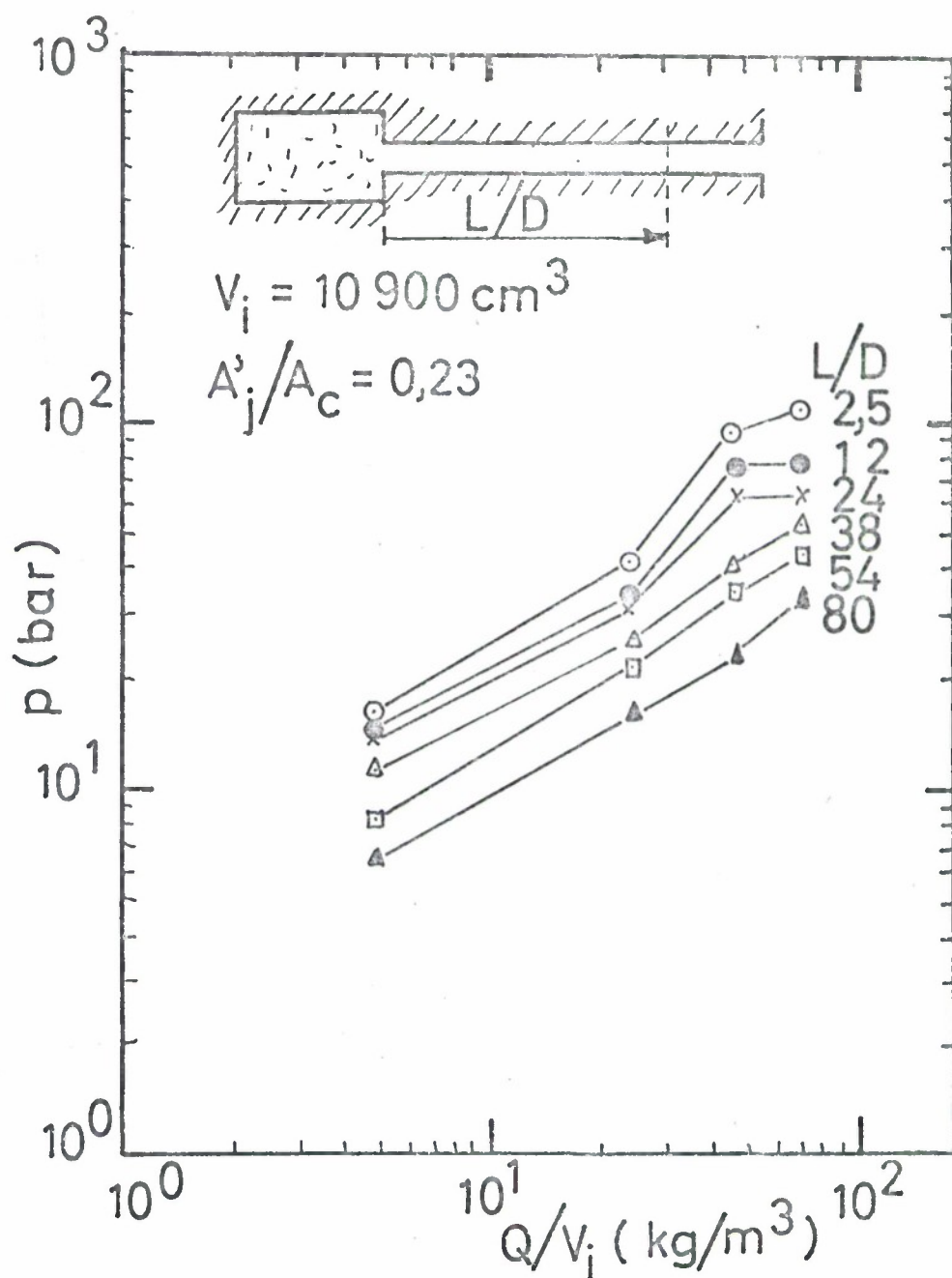


Fig. 4.2b. Peak pressure versus chamber loading density with  $L/D$  as parameter for the same test configuration as in Fig. 4.2a.

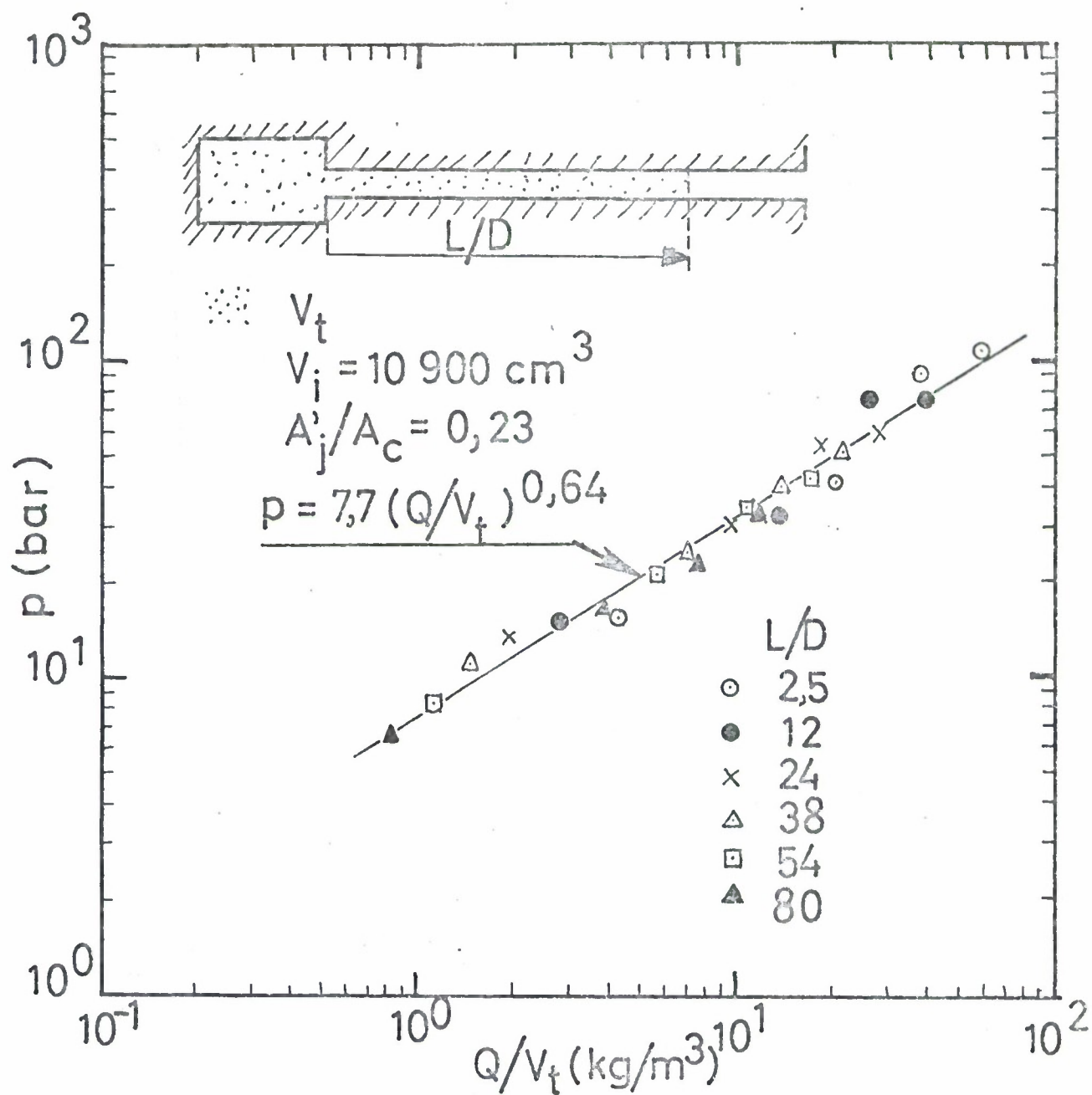


Fig. 4.2c. Peak pressure versus effective loading density for the same test configuration as in Fig. 4.2a and 4.2b. The solid line represents the least squares fit to all the data.

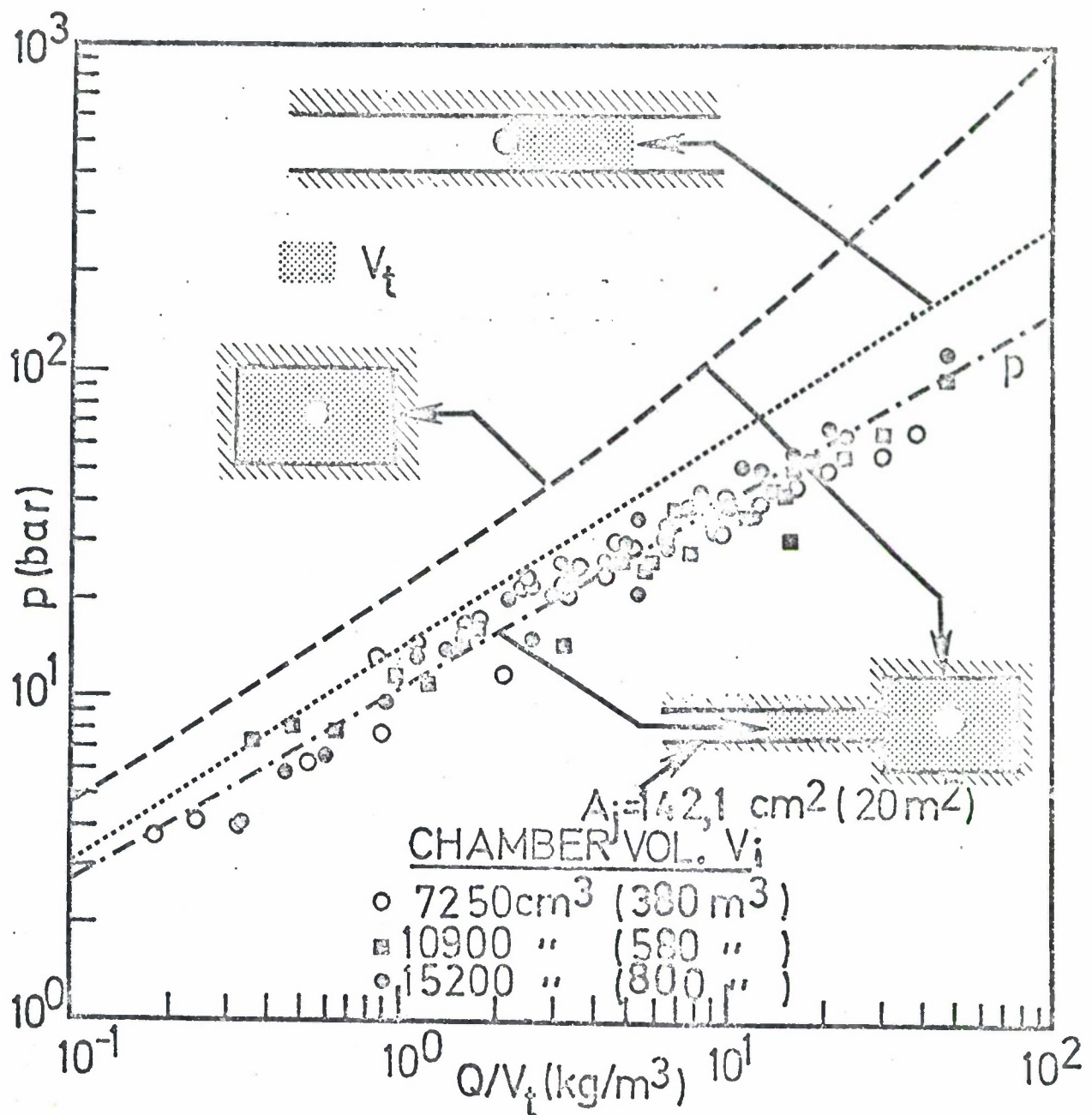


Fig. 4.2d. Peak pressure versus effective loading density in single chamber storage sites for three chamber volumes. The ratio between the tunnel and chamber cross-sections is  $A_j/A_c = 0,45$ . The numbers in parentheses refer to typical full scale sites. The results from model tests in closed chambers /2/ and in straight tubes /7/ are also included in the figure.



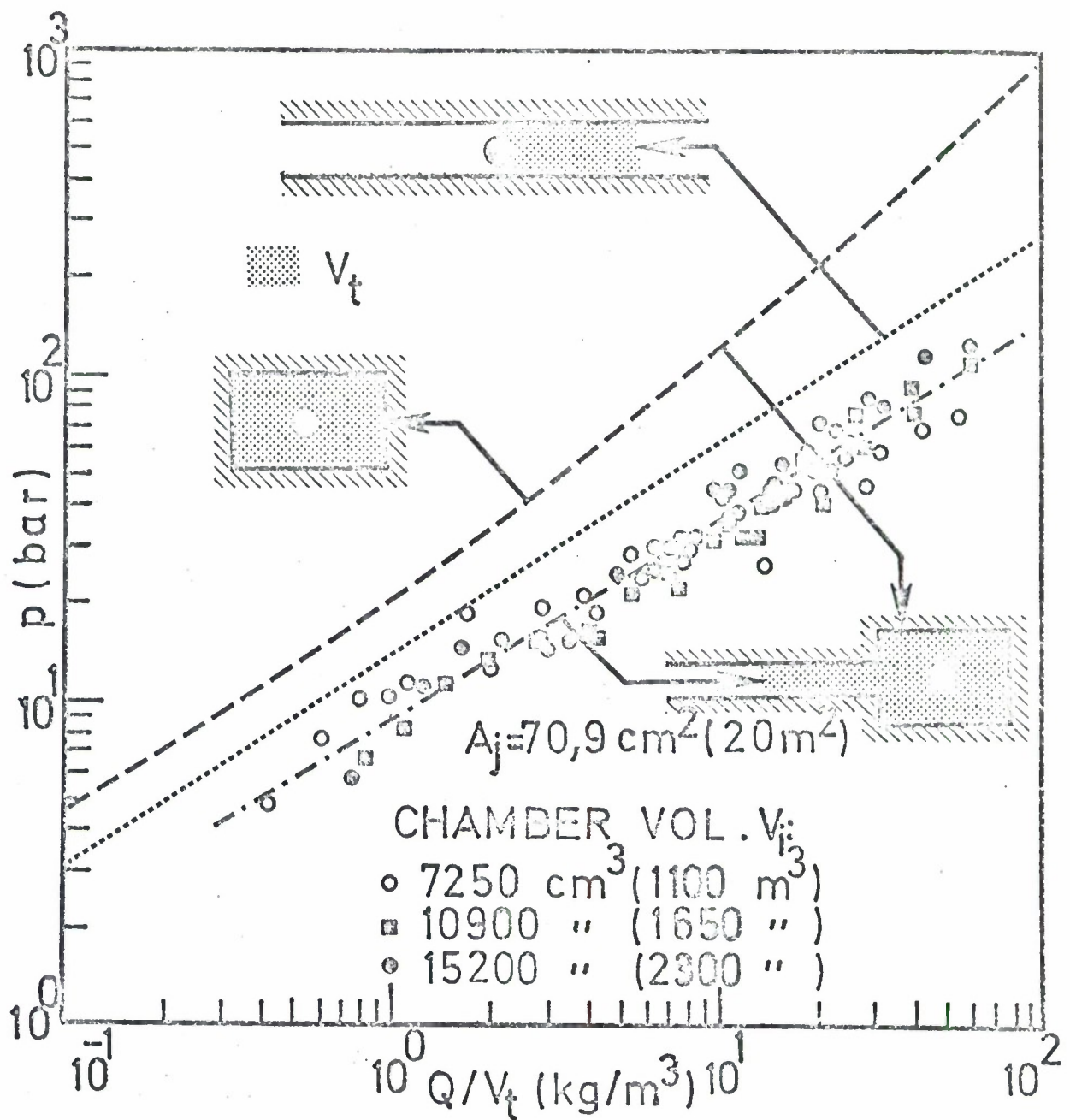


Fig. 4.2e Peak pressure versus effective loading density for  $\Lambda_j/\Lambda_c = 0,23$  (See Fig. 4.2d for details).

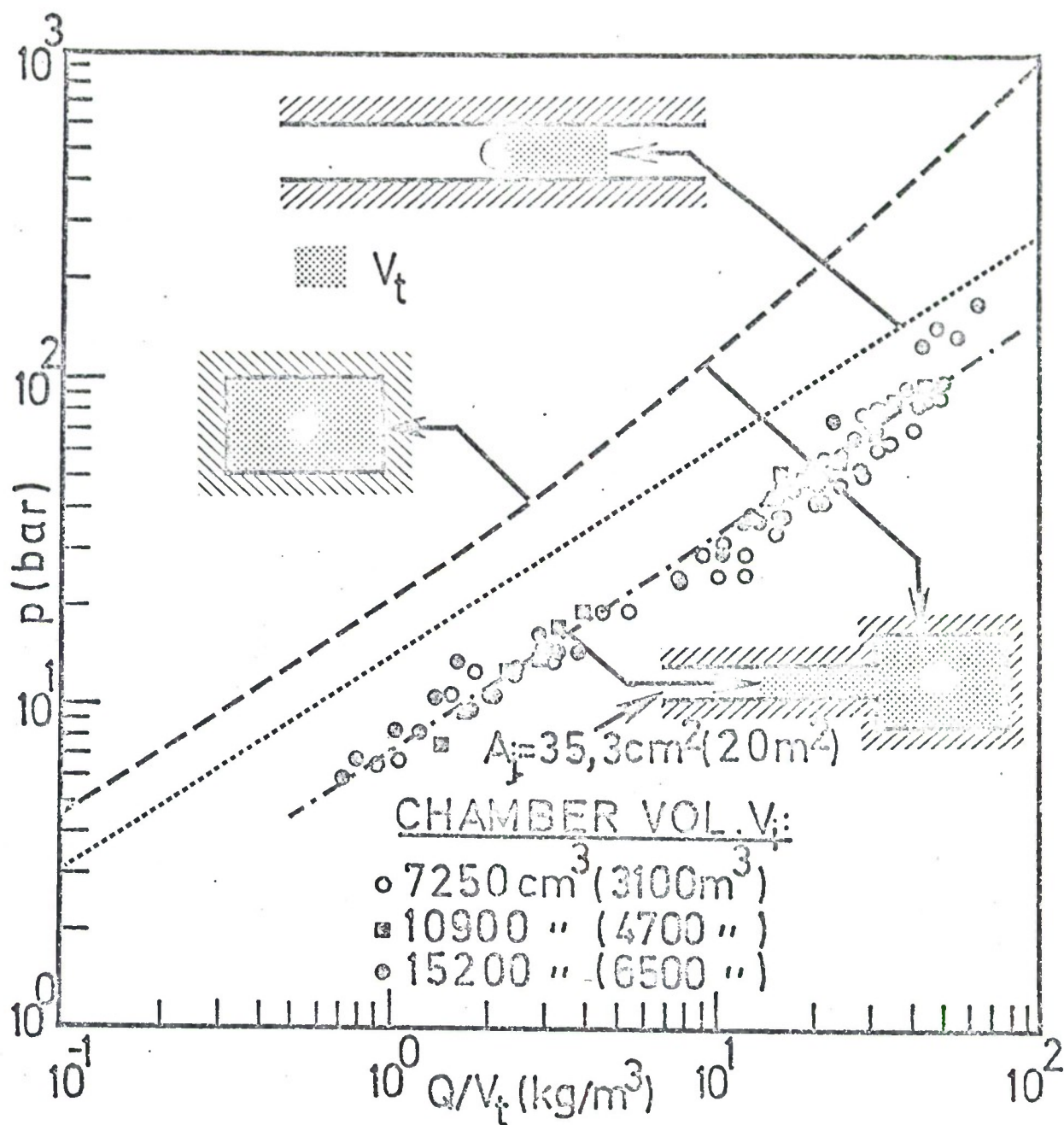


Fig. 4.2f. Peak pressure versus effective loading density for  $A_j/A_c = 0,11$ . (See Fig. 4.2d for details).

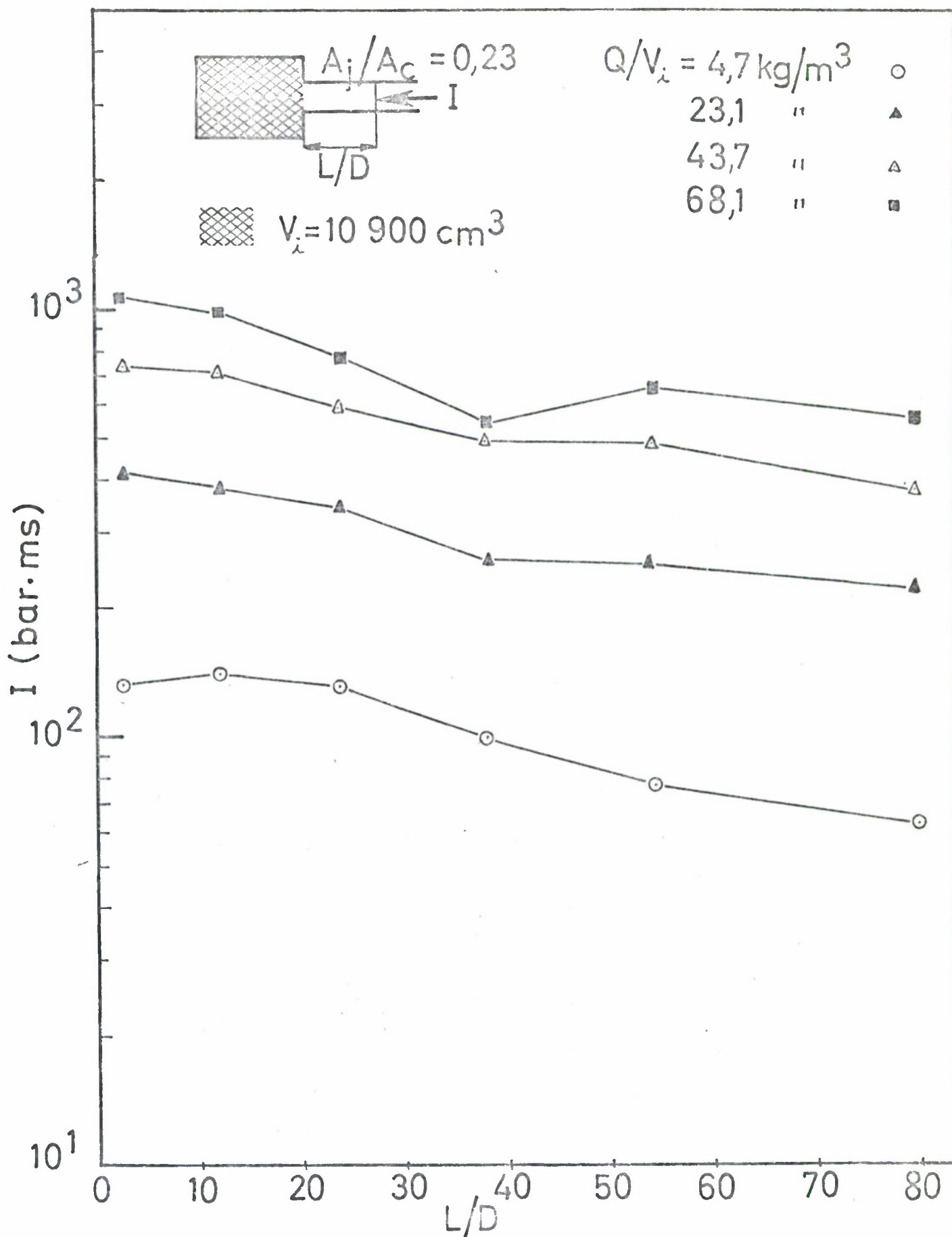


Fig.4.3a.Example of positive impulse versus distance from chamber exit expressed in tunnel diameters.



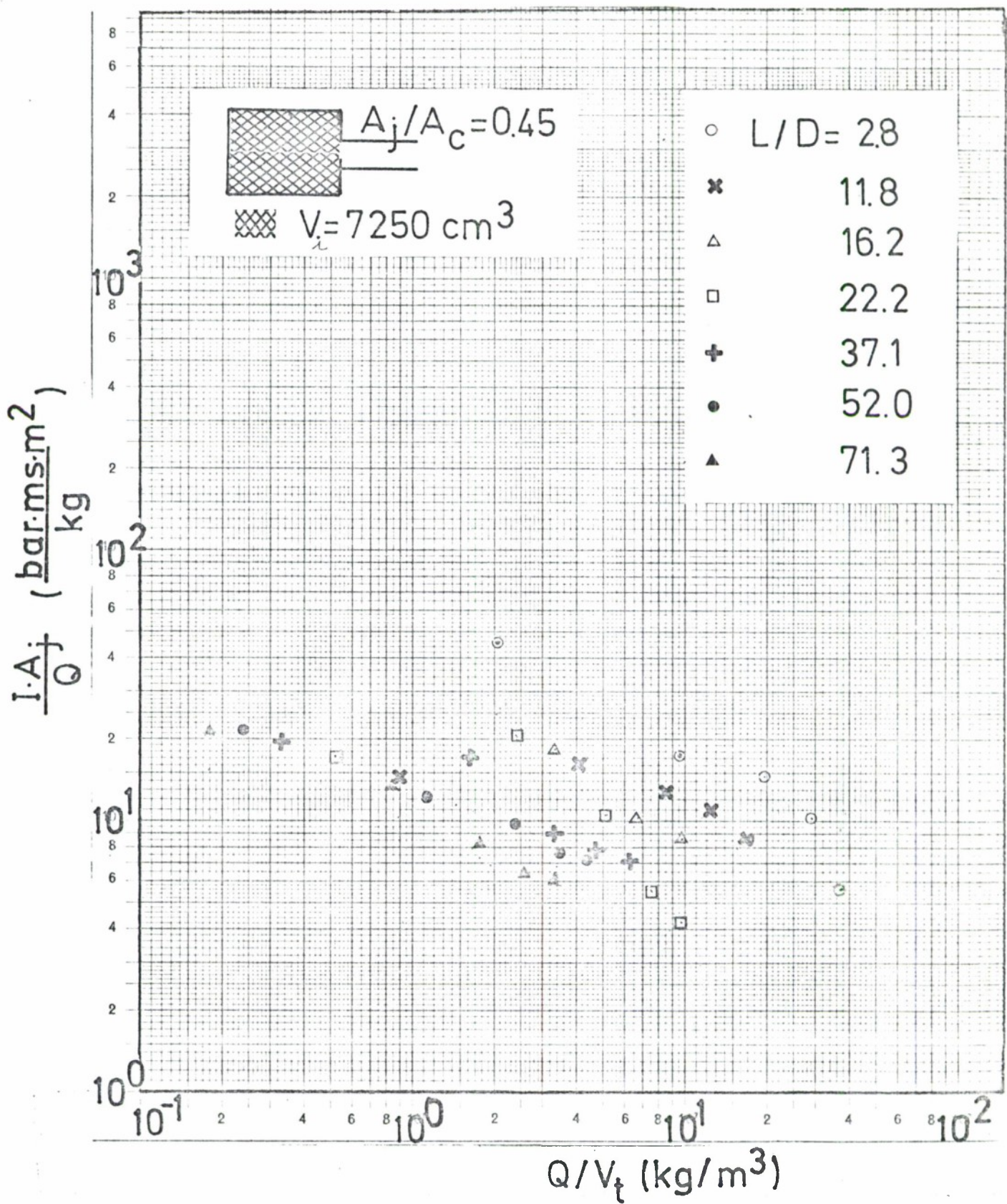


Fig. 4.3b Scaled impulse versus effective loading density [Eq.(2.1e)] at various distances in tunnel diameters from the chamber exit.



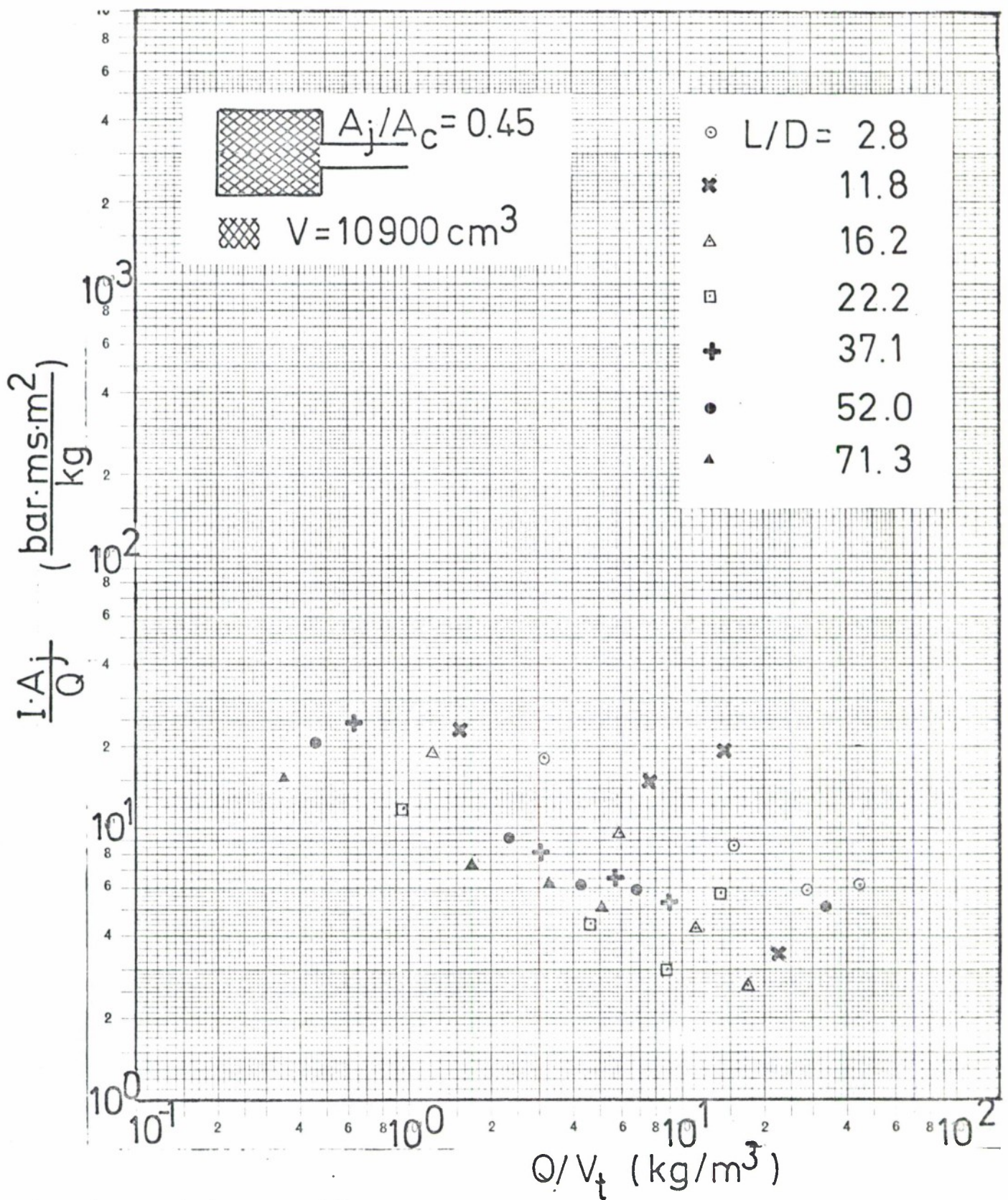


Fig. 4.3c Scaled impulse versus effective loading density [Eq.(2.1e)] at various distances in tunnel diameters from the chamber exit.



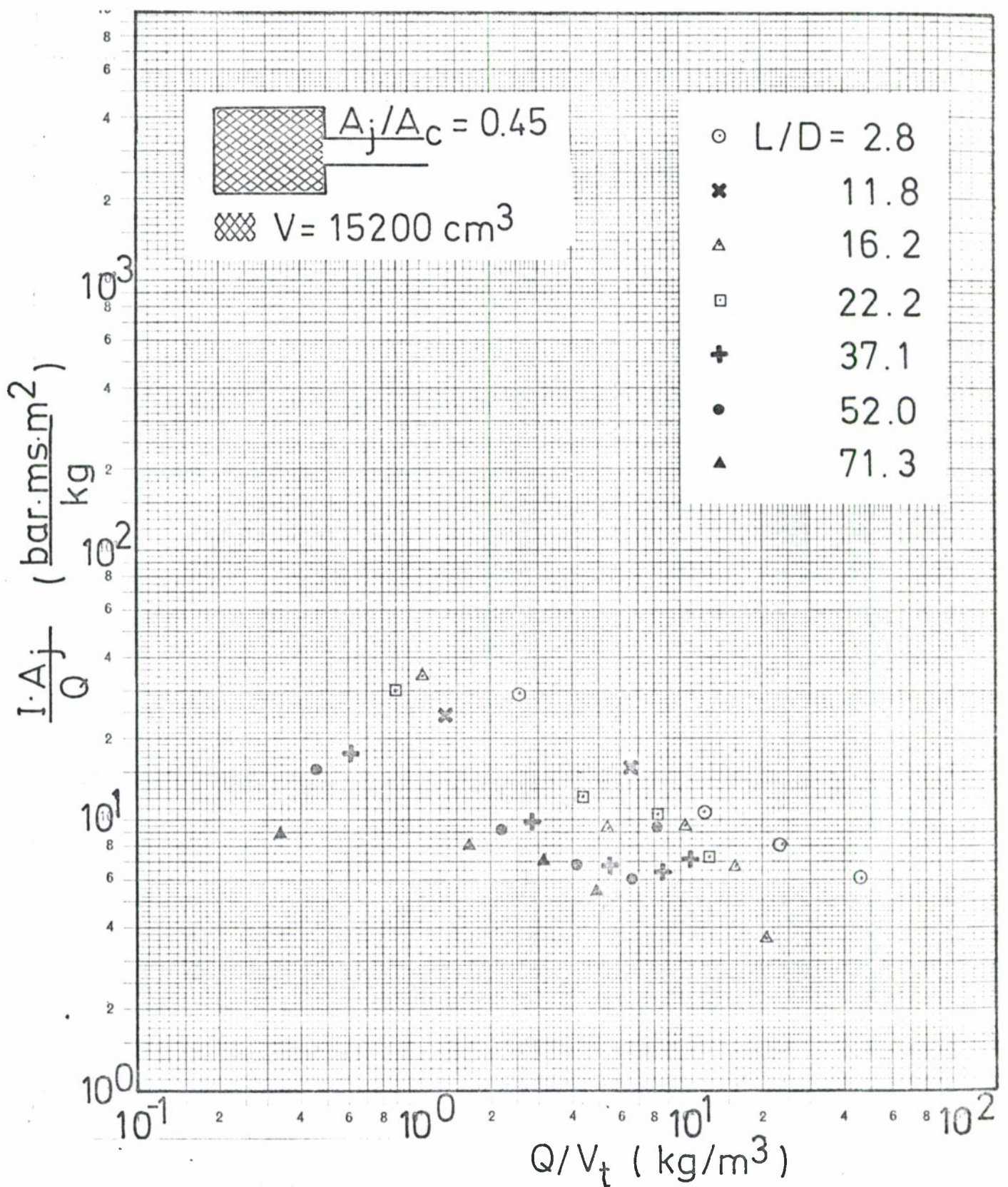


Fig. 4.3d Scaled impulse versus effective loading density Eq.(2.1e) at various distances in tunnel diameters from the chamber exit.



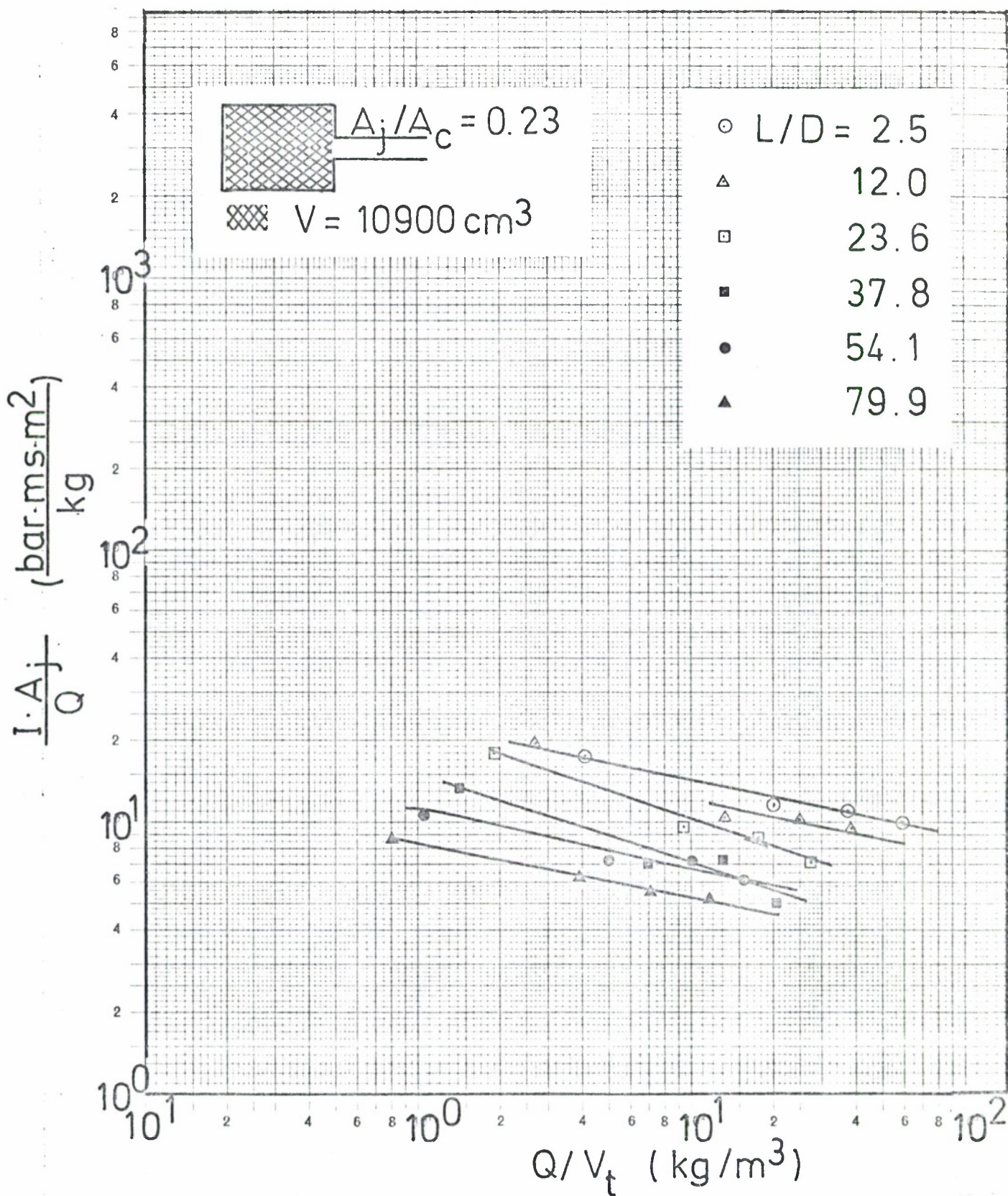


Fig. 4.3e Scaled impulse versus effective loading density [Eq.(2.1e)] at various distances in tunnel diameters from the chamber exit.



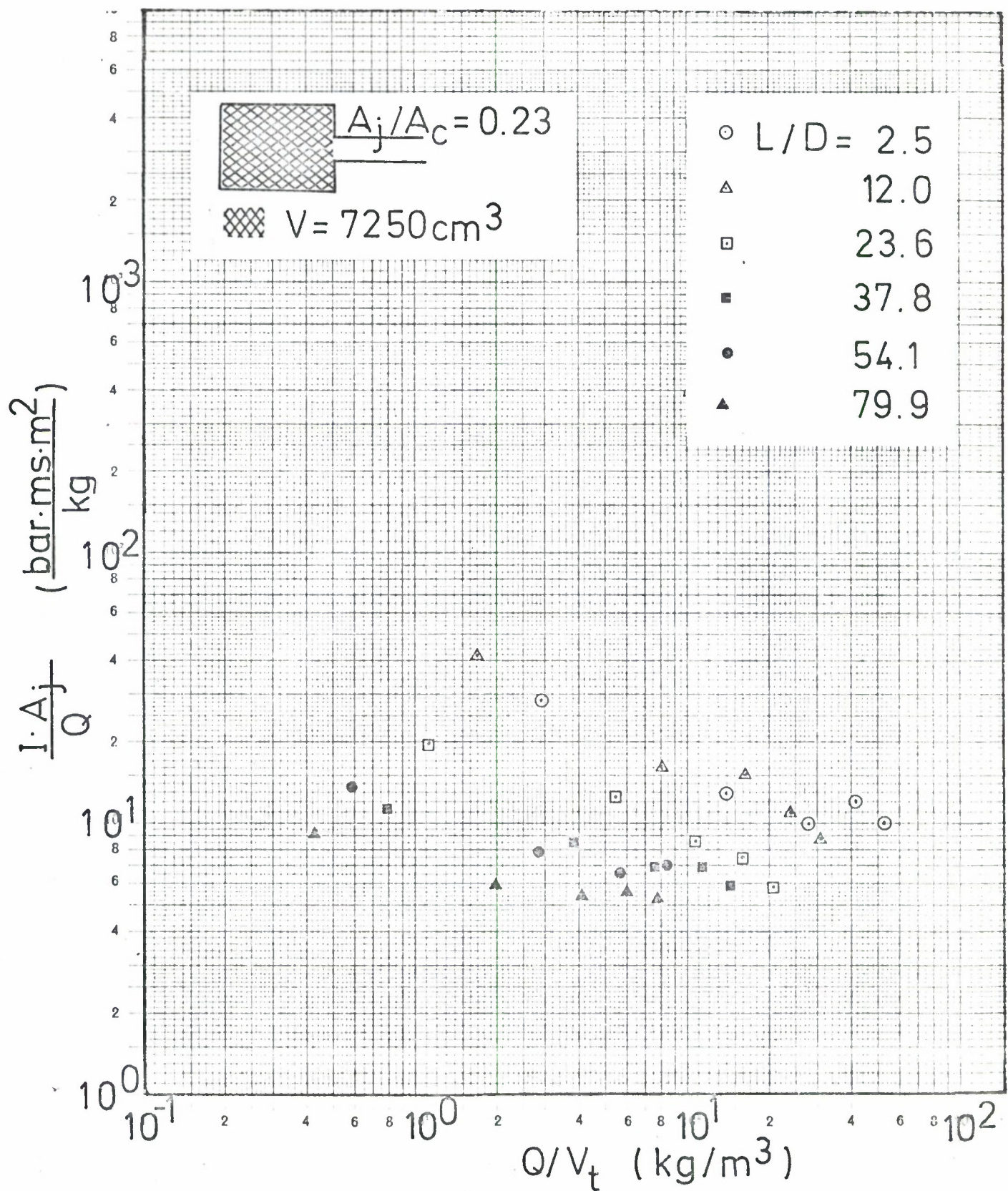


Fig. 4.3f Scaled impulse versus effective loading density [Eq.(2.1e)] at various distances in tunnel diameters from the chamber exit.



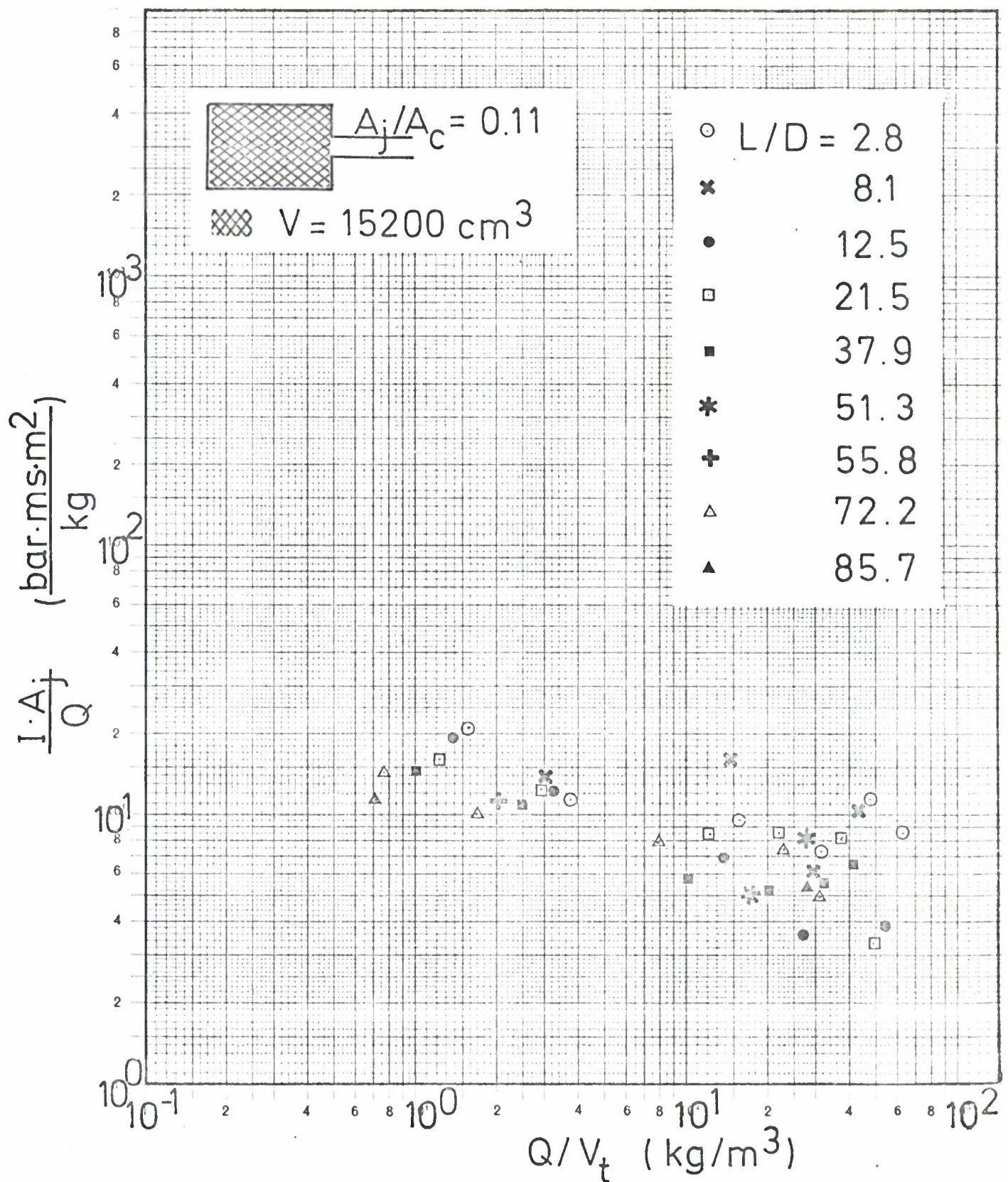


Fig. 4.3g Scaled impulse versus effective loading density [Eq.(2.1e)] at various distances in tunnel diameters from the chamber exit.

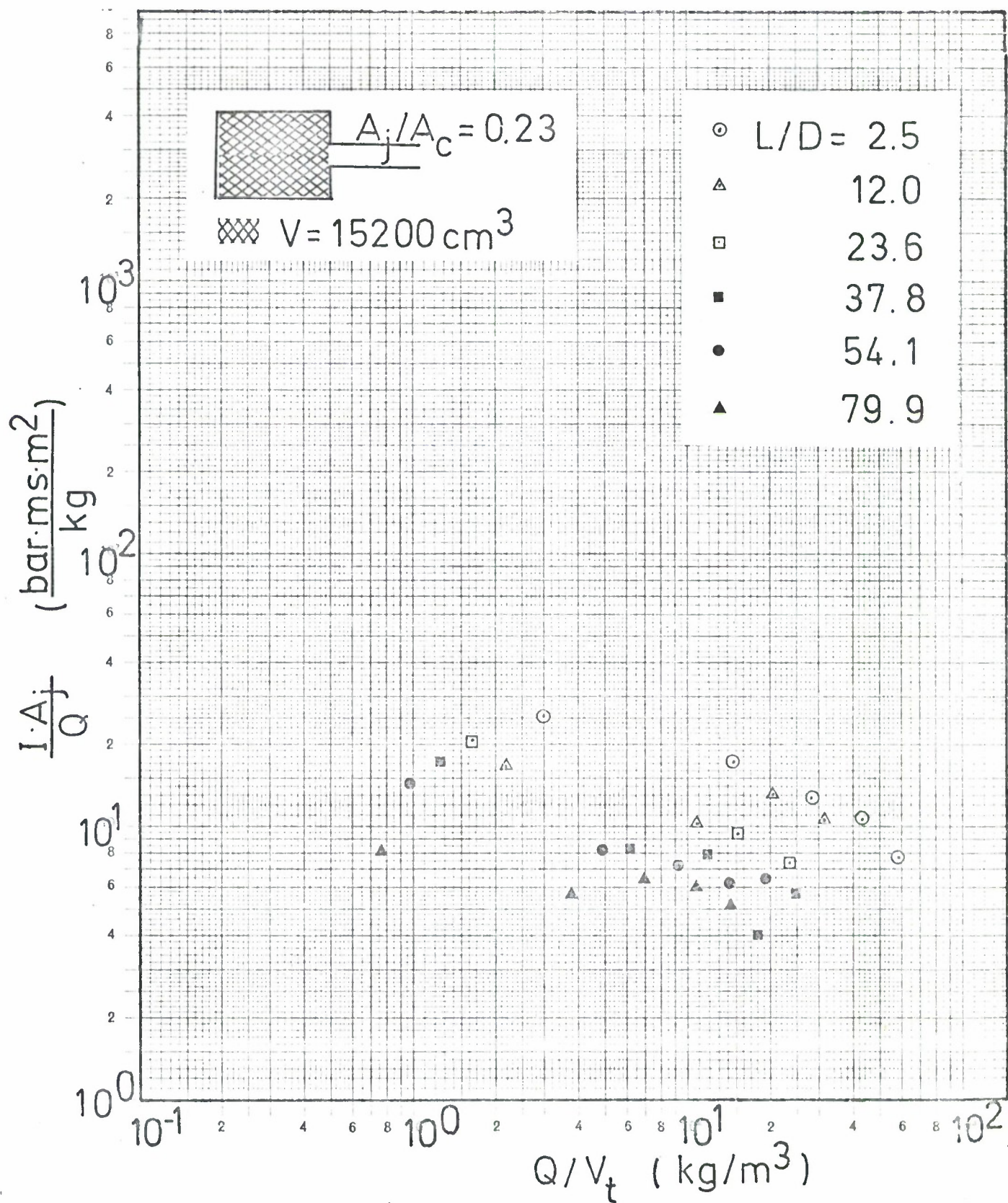


Fig. 4.3h Scaled impulse versus effective loading density [Eq.(2.1e)] at various distances in tunnel diameters from the chamber exit.



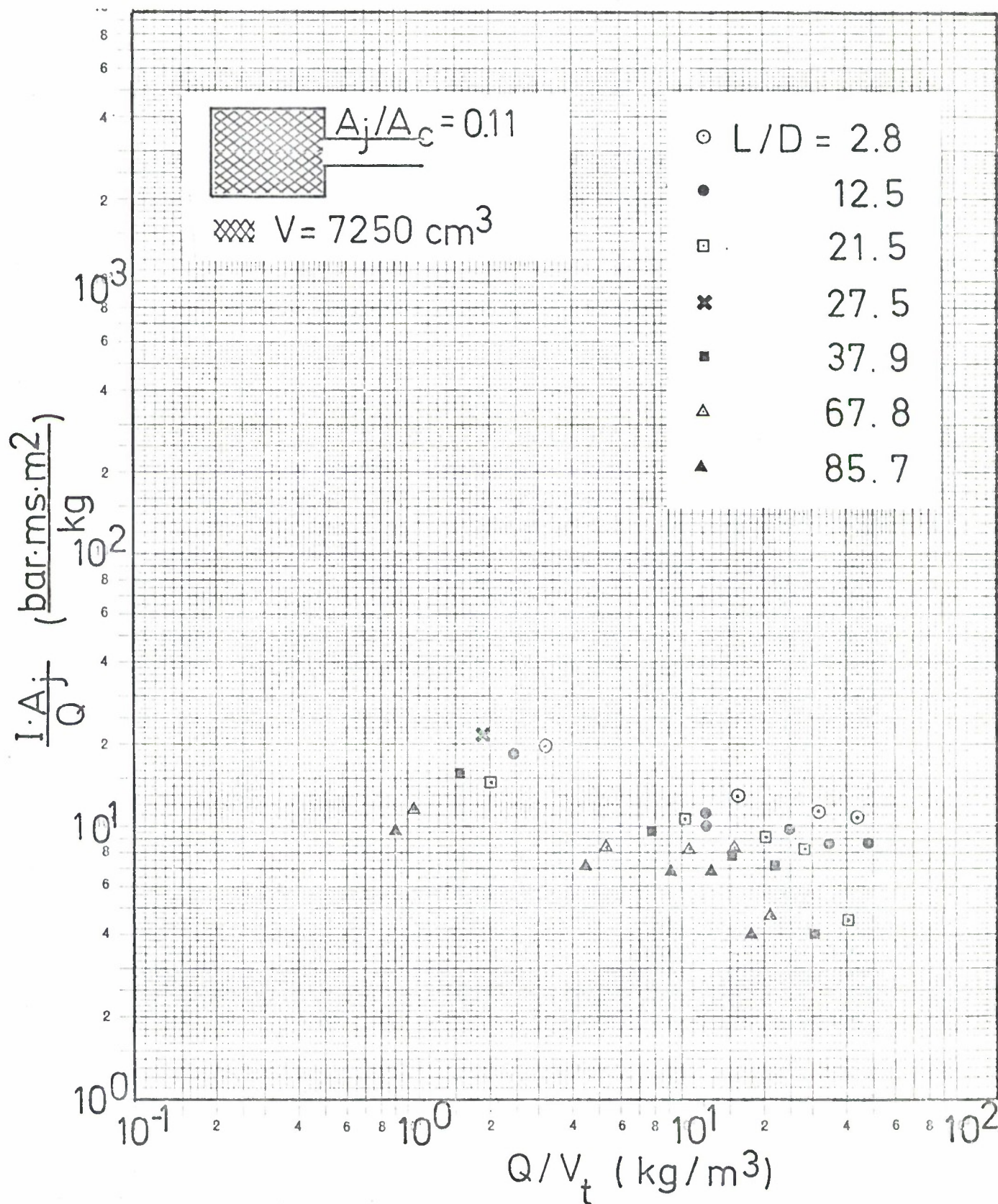


Fig. 4.3i Scaled impulse versus effective loading density [Eq.(2.1e)] at various distances in tunnel diameters from the chamber exit.

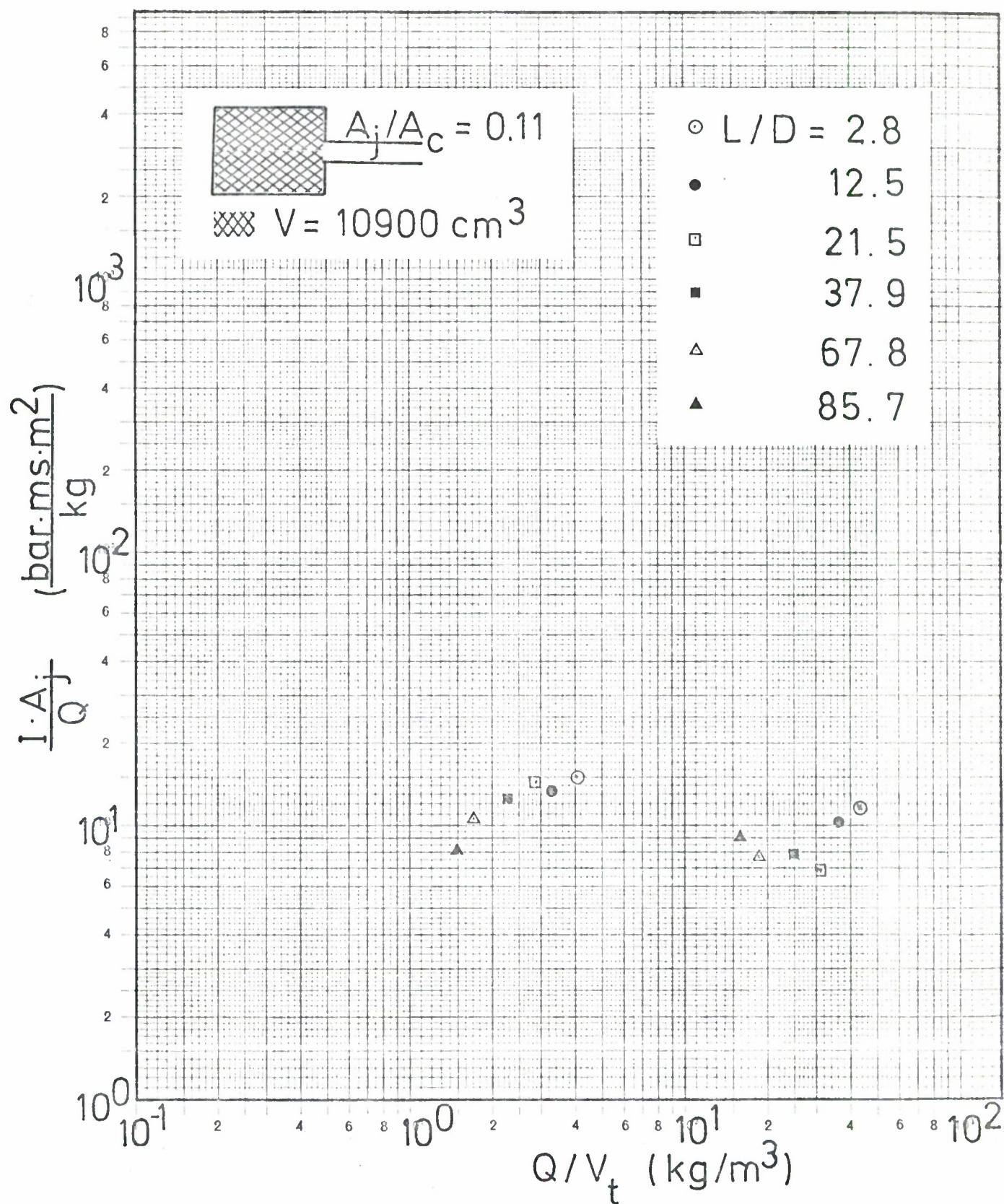


Fig. 4.3j Scaled impulse versus effective loading density [Eq.(2.1e)] at various distances in tunnel diameters from the chamber exit.



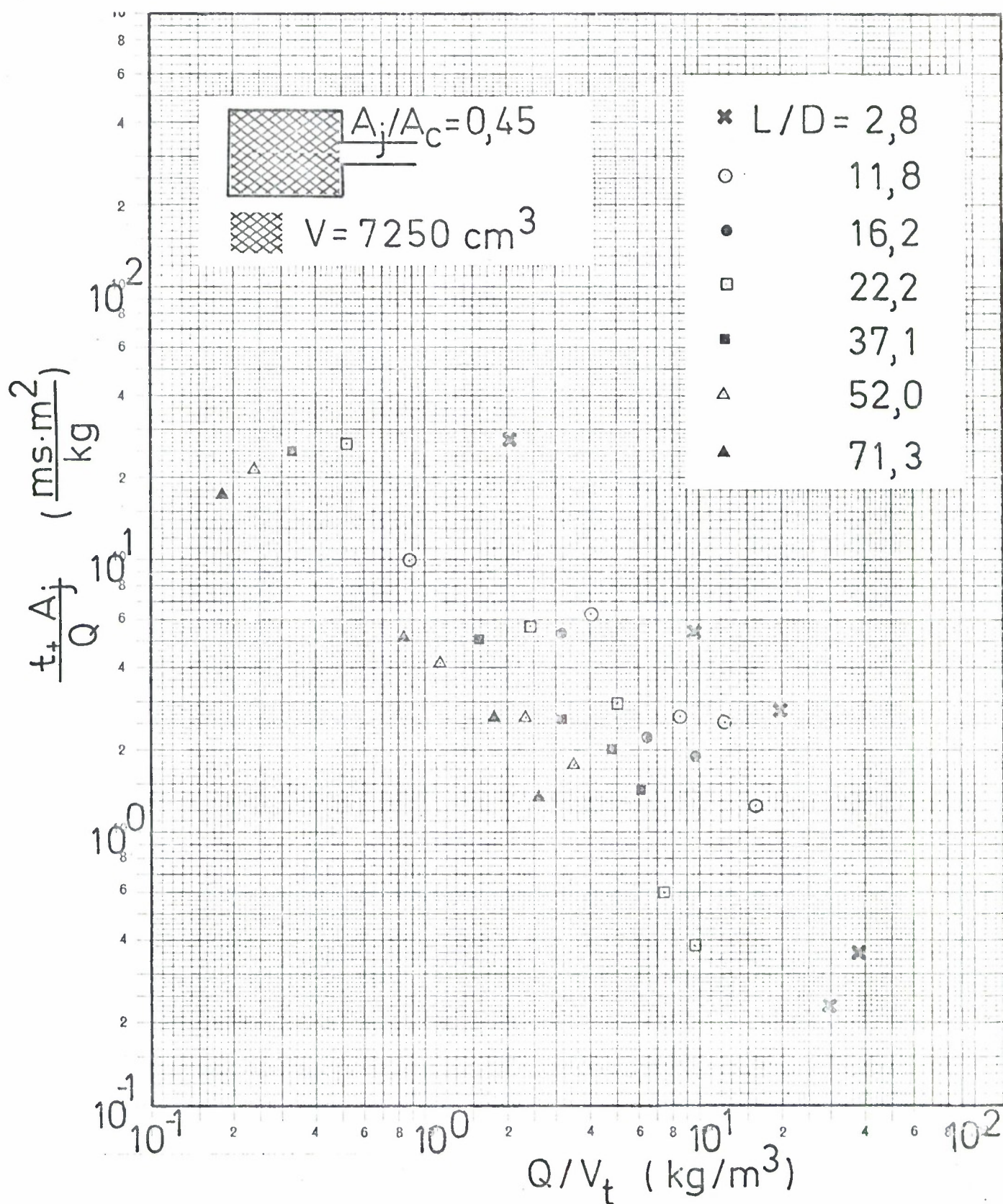


Fig. 4.3k Example of scaled positive duration versus effective loading density [(Eq.(2.1f))] at various distances in tunnel diameters from the chamber exit.

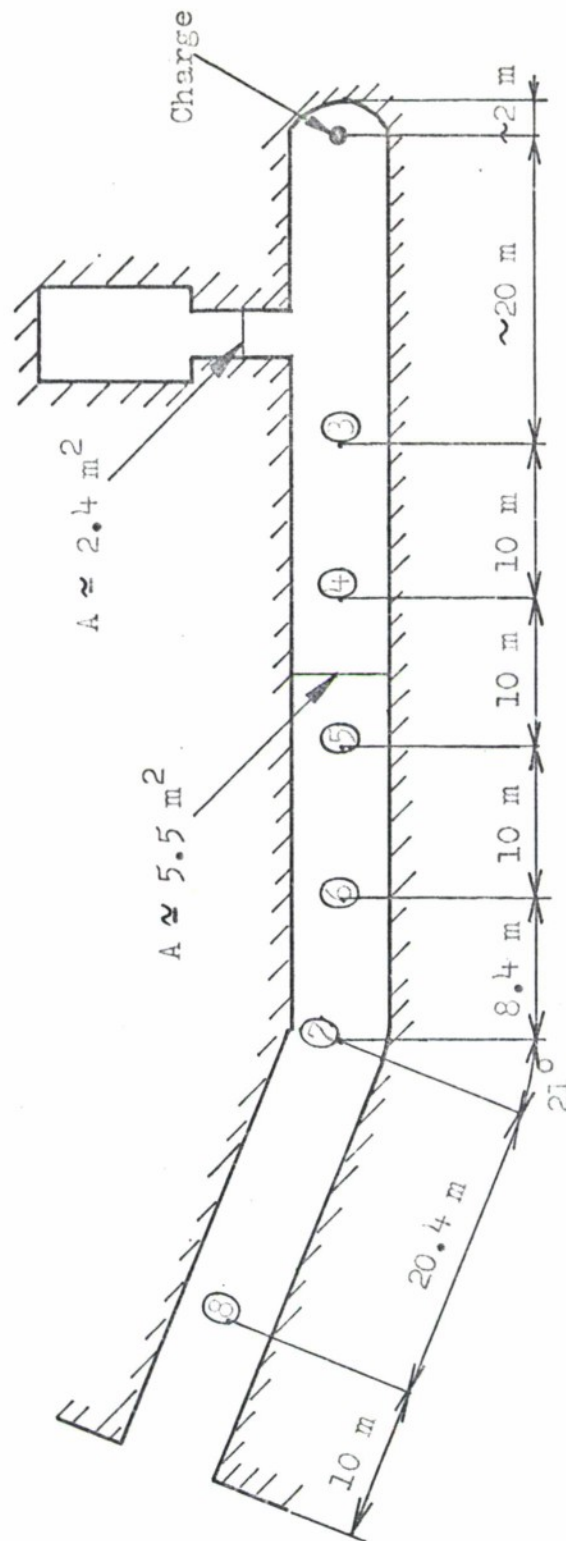


Fig. 4.5a Tunnel system in the scale tests performed by NDRE /13/.



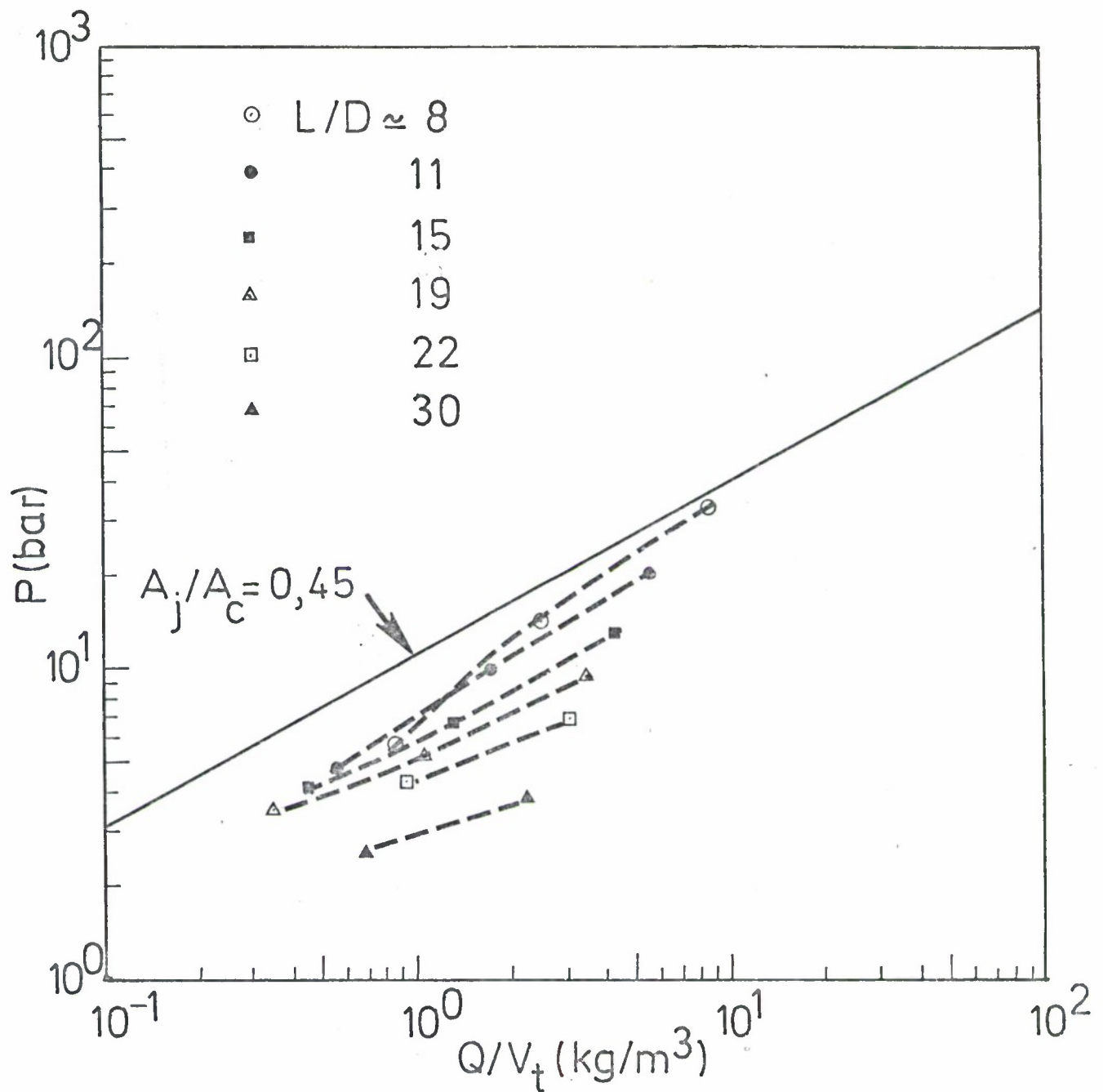


Fig. 4.5b Peak pressure versus effective loading density for the large scale tests performed by NDRE /13/ in comparison with the model data for  $A_j/A_c = 0.45$ . The  $L/D$ -dependence is consistent with an average wall roughness of approximately 0,2 m.

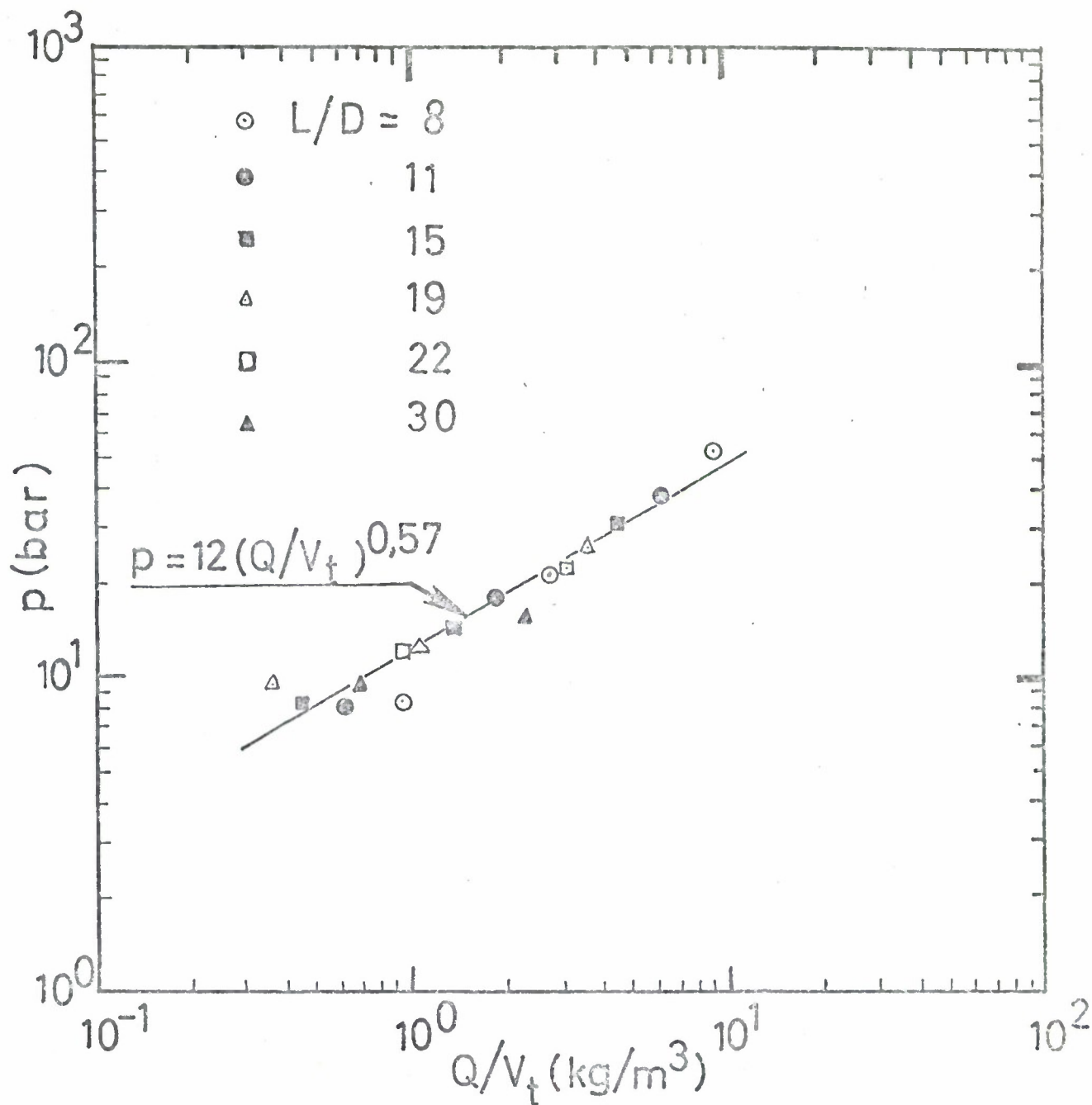


Fig. 4.5c. "Smooth wall" peak pressure  $p_o$  versus effective loading density for the large scale test data in Fig. 4.5b.